Universität Hamburg

Commissioning of the Readout Electronics for the Prototypes of a Hadronic Calorimeter and a Tailcatcher and Muon Tracker

Diplomarbeit

von

Benjamin Lutz

Institut für Experimentalphysik
Universität Hamburg

Mai 2006

Abstract

The goal of the CALICE collaboration is to develop and design a highly granular calorimeter for an experiment at the future international linear collider. In an integrated study all parts of the calorimeter are considered. Within this project a hadronic calorimeter prototype, built at DESY, and a tailcatcher and muon tracker prototype, built at NIU and Fermilab, are developed.
The subject of this thesis is the combined readout electronics for these prototypes. In a set of measurements it is demonstrated that the individual components answer their purposes. This includes the classification of noise, linearity and signal to noise ratio of the amplifier and a study of the differential nonlinearity of the analog to digital converter in the data acquisition. In addition to these measurements of common parameters, some attributes are measured that are special to the use of the combined system, including the influence of the limited time resolution of the hold signal and the consequences of signals with variable input signal shape.
Furthermore, an algorithm is developed for the determination of the SiPM gain from single photo-electron spectra that are recorded with the detector readout electronics. Particular effort is made to ensure that the developed method can be run independently from human intervention, as a 8000 channel system demands. The accuracy and stability of the gain measurement is checked with actual data from the first available hadronic calorimeter modules and a set of requirements for a measurement of 1% accuracy is fixed. Finally, the established gain measurement is used in the calibration of modules with cosmic muons. And the temperature dependence of the SiPM gain is verified.

Zusammenfassung

Die CALICE Kollaboration hat sich die Entwicklung und Realisierung eines hoch auflösenden Kalorimeters für den geplanten internationalen Linearbeschleuniger zum Ziel gemacht. Sämtliche Teile des Kalorimeters werden in einer Projektstudie untersucht. Neben einem hadronischen Kalorimeter Prototypen der am DESY konstruiert wird, wird außerdem ein Prottotyp eines "Tailcatcher" und Myon Tracker an der NIU und am Fermilab konstruiert.
Diese Arbeit beschäftigt sich mit der gemeinsamen Ausleseelektronik für diese Prototypen. In einem Satz von Messungen wird gezeigt, daß die einzelnen Komponenten ihren Zweck erfüllen. Dies schließt sowohl die Bestimmung des Rauschens, der Linearität und des Signal-Rausch-Abstandes des Verstärkers so wie die Untersuchung der differenziellen Nichtlinearität der Analog-zu-Diigital-Wandler ein. Zusätzlich zu diesen allgemeinen Parametern werden einige Besonderheiten des integrierten elektronischen Systems einschließlich des Einfluß der begrenzten Zeitauflösung des "hold"-Signals und der Einflüsse von unterschiedlichen Eingangsignalformen untersucht.
Des weiteren wird ein Algorithmus für die Messung der SiPM Verstärkung entwickelt, der diesen Wert aus den mit der Ausleseelektronik aufgenommenen Photoelektronenspektra bezieht. Um eine effiziente Messung in einem System mit 8000 Kanälen zu erreichen, wird besonderer Wert auf Lauffähigkeit unabhängig von Benutzereingriffen gelegt. Die Zuverlässigkeit und Genauigkleit der Methode wird anhand von Daten, die mit der dem ersten hadronischen Kalorimetermodul genommenen wurden, getestet. Auch werden die notwendigen Bedingungen für eine Messung mit einprozentiger Genauigkeit festgelegt. Abschließend wird die entwickelte Methode zur Messung der Verstärkung in einem Aufbau zur Kalibrierung mit kosmischen Myonen benutzt. In dieser Messung wird auch die Temperaturabhängikeit der SiPM-Verstärkung bestätigt.

Contents

Introduction

The desire to understand the world right down to the last detail has always been intrinsic to the nature of mankind. Over the last century, particle physics has extraordinarily contributed to the understanding of matter itself and the forces which "hold the world together in its inmost folds" [Goethe]. The experiments performed in high energy physics over the last decades gave rise to a formalism called the Standard Model (SM) of particle physic describing the laws that govern our world. Though still one particle predicted in this theory, the Higgs, was not observed in the energy range accessible today. To see if the SM holds or to understand how it has to be extended accelerator machines capable of reaching new energy limits are needed.

Two projects, the Large Hadron Collider (LHC) realized at the moment, and a planned electron-positron linear collider have the potential to reach energies in the necessary range.

Since summer 2004, with the decision upon the accelerator technology a time-line has been established for the realization of a future e^+-e^- linear collider, the International Linear Collider (ILC). The release of the ILC Reference Design Report is planned for the end of 2006. Next to the development of the accelerator technology, the development of the required detector technologies for such a collider is in full swing. Among several activities all over the world, a hadronic calorimeter (HCAL) prototype is built at DESY[1].

To realize the required energy resolution, the ILC detector follows the particle flow concept. The detector has to be capable to track the particles through the full volume in this concept. This requires the development of new detector hardware with high spacial resolution, especially for the calorimeters.

The CALICE collaboration, consisting nowadays of 35 institutes from nine countries, connects the studies on prototypes for electromagnetic and hadronic calorimeters as well as for a tailcatcher and muon tracker. Special effort is put into the development and comparison readout concepts for the hadronic calorimeter.

Within the collaboration a fine segmented steel-scintillator HCAL prototype is built at DESY. For the technical realization of such a calorimeter the novel silicon based photodetector developed at MEPhI[2], called Silicon Photomultiplier (SiPM), has several advantages and was chosen for the prototype. The same photodetectors are used in the prototype of a tailcatcher and muon tracker (TCMT) prototype which is developed by NIU[3] and Fer-

[1]Deutsches Elektronen Synchrotron
[2]Moscow Engineering Physics Institute
[3]Northern Illinois University

milab[4] in cooperation with DESY. The realization of the prototypes is the first large scale usage of SiPMs. A standard design for the readout electronics of these devices does not yet exist and thus an extensive knowledge of the interaction between detector and dedicated readout electronics is necessary.

The first chapter of this thesis describes the detector technology planned for the ILC including the constraints which the use of particle flow has on the choice of the technology. Special emphasis is put on the physical and technical limitations of calorimeter measurements and how the particle flow algorithm tries to minimize the their influence. Furthermore the research program of the CALICE collaboration is introduced.

The general part covering calorimetry is followed in chapter 2 by a detailed description of the signal creation and processing in the HCAL and TCMT prototypes. The full readout chain, from the particle creating a signal in the scintillator to the digitization in the data acquisition system, is described with special focus on the signal creation in the SiPM and the amplifier technology.

In the third part a set of measurements is described, which were performed to ensure that the readout electronics fulfills the requirements. This includes the determination of the amplifier gain and noise as well as the determination of its linear range and the dependence on the input signal shape. In addition the attributes of the data acquisition like noise and the differential nonlinearity of the analog to digital conversion were studied. Based on this measurements the adaptation between amplifier and analog to digital converter was optimized.

The fourth chapter describes the development of an algorithm to distinguish the SiPM gain from single photoelectron spectra recorded with the detector readout system. Next to the development of a proper mathematical description, effort is put into the development of software capable of automatic running. This is necessary as the 8000 channels of the prototype should be calibrated with a minimum of human intervention. The influences of the differential nonlinearity in the data acquisition system and systematic dependencies on the amount of light, used for the calibration, are studied. The gain measurements studies are concluded with the determination of the minimal requirements in statistics and a first application with the detector prototype.

[4]Fermi National Accelerator Laboratory, Chicago, Illinois

Chapter 1

Calorimetry at the International Linear Collider

1.1 International Linear Collider (ILC)

The research and development described in this thesis are made in the context of the planned electron-positron linear collider, the International Linear Collider (ILC) project.

At the moment, the Large Hadron Collider (LHC), which is built at CERN[1] near Geneva, is the latest and most promising project of the accelerator based high energy physics to open the frontier for new discoveries. One of the most "popular" particles the LHC should find is the Higgs, the last not observed particle in the Standard Model of Particle Physics. The LHC is a ring hadron collider, which makes it feasible to reach an energy range up to 7 TeV per beam, with the currently available accelerator technique.

The use of hadrons gives on one hand the possibility to use a ring collider, as the synchrotron radiation scales with $\propto \frac{E^4}{m_0^4}$ and shifts the limit of achievable energies to much higher energies as it could be reached for leptons. But on the other hand hadrons are compound objects, consisting of quarks and gluons and give a less defined initial condition than a lepton pair would give. The background and radiation is also a big challenge for the LHC.

A linear accelerator does not suffer from the synchrotron radiation problem, so that an electron positron accelerator can be built, which reaches up to 1 TeV center of mass energy. The technology, which is foreseen for the ILC, is tested and already used in the Free Electron Laser (FEL) project at DESY[2]. Lepton-antilepton collisions give a much cleaner environment for the creation process of new particles than hadron collisions. This makes the ILC a very precise instrument not only to verify and increase the precision of LHC but also to complement it.

[1] Conseil Eropéen pour la Recherche Nucléaire
[2] Deutsches Elektronen Synchrotron

1.2 Detector Concept for the ILC

A detector concept for the ILC has to ensure, that the possibilities of such a machine are met by the precision of the measuring device. The physics program foreseen for the ILC requires an unprecedented accuracy of the detector.

The concepts proposed follow the established structure of particle detectors with a vertexing system giving a high spacial resolution near the interaction point followed by a main tracker either TPC or silicon tracker for the measurement of trajectory and thus momentum of charged particles. The tracking system is surrounded by an electromagnetic and hadronic calorimeter to measure the energy of the particles. Outside the magnet, that generates the field for the tracker measurements, a muon tagger and tracker completes the detector.

To achieve the envisaged accuracy the detector concepts follow the "particle flow" algorithm, where each particle is tracked through the detector separately as long as possible. This sets new constraints especially on the design of the calorimeters. A very fine granularity and individual readout of the calorimeter cells is necessary. At the same time, the calorimeter system has to be placed inside the magnet to avoid a reduction of the resolution by not recognized interactions in the coil.

An example for a possible detector is the Large Detector Concept which is shown in figure 1.1 together with the simulated detector signals for the decay of a Z^0.

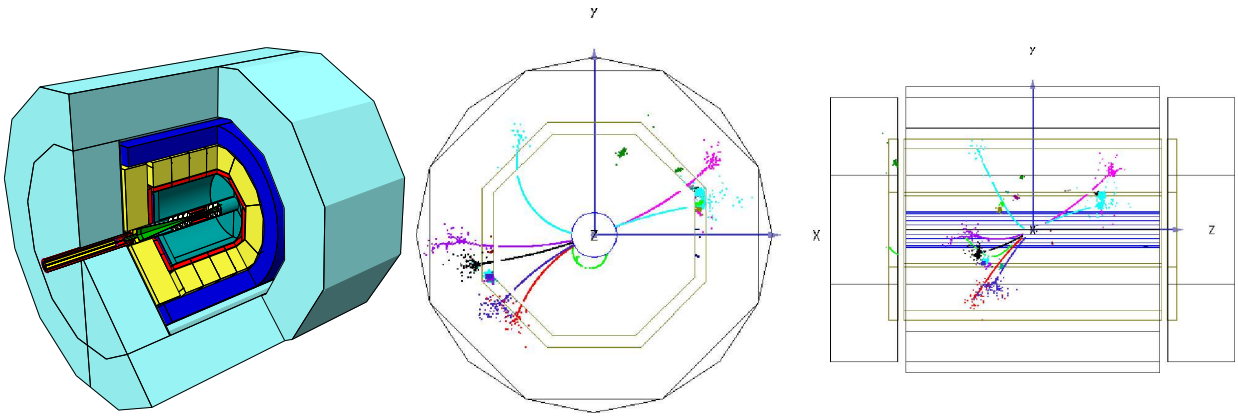

(a) LDC (b) Front view of a decaying Z^0 (c) Side view of a decaying Z^0

Figure 1.1: Sketch of the Large Detector Concept (LDC) proposed for the ILC and a simulated Z^0 decay

1.2.1 Calorimetry

Whereas tracking devices try to measure a particle without changing its identity and try to "touch" it as little as possible, a calorimeter measures the energy of a particle without preserving the particle itself. The goal is to measure the full energy of the particle by absorbing it in a dense material and assuming that the energy deposited is the energy of the particle, applying the law of energy conservation.

The processes which lead to the absorption of particles in matter are manifold: ionization; excitation of atoms, molecules or nuclei; emission of Cherenkov light; creation of δ-electrons; bremsstrahlung; nuclear reactions; hadronic reactions; neutron caption; nuclear fission.
In many of these processes photons are created, which themselves are absorbed by: photoelectric effect; Rayleigh scattering; Compton scattering; pair production; photonuclear reactions.

For a true application of the energy conservation law it would be necessary to sum over all the individual energy deposits. This is for sure not possible in a technical realization of a calorimeter. Not all energy deposits can be measured with the same method. In addition one does not want to integrate too much noise, this cuts processes where the energy is released comparably late with respect to the primary interaction. Another limitation with respect to energy conservation is the fact, that often calorimeters are not sensitive over the full volume. Sampling calorimeters, where a material with high atomic mass like W, Pb, U, Fe or Cu is interleaved with sensitive material, e. g. scintillator or gas, read only the energy deposited in the fraction of the sensitive volume. This means, that one has to distinguish the relation between absorbed and measured energy, the response function, for an actual calorimeter.

The quality of a calorimeter measurement is defined by the fluctuations in the measured signal, the energy resolution.

Electromagnetic Showers

Neglecting hadrons, a typical electromagnetic shower is initiated by a highly energetic $e^{\pm}$ or photon. The most dominant processes at $e^{\pm}$ energies over 1 GeV is bremsstrahlung. The average distance on which these particles looses $1 - \frac{1}{e} = 63.2\%$ of its energy is called the radiation length X_0. Pair production is the most probable process for photons with high energies (>1 GeV). The mean free path for very high energetic photons is $\lambda_{photon} = \frac{9}{7} X_0$.

The fact, that electrons can produce high energetic photons and these photons produce electron positron pairs, which themselves can radiate photons again, gives rise to a cascade of particle multiplications. The number of photons, electrons, and positrons increases. This continues as long as the average energy of the shower particles is larger than the critical energy E_c. At lower energies Compton scattering and photoelectric effect start to dominate, which convert one photon to one electron and the $e^{\pm}$ loose their energy mainly through ionization. The energy at which the average losses due to ionization and radiation

are equal is called the critical energy. After E_c is reached, the number of particles in the shower, and thus the energy deposited reduces until the shower dies out.

Clearly, the shower does not only grow in depth, it will also show a distribution transverse to its main axis. The radius of the cylinder in which 90% of the energy is deposited is called Molière radius $\rho_M = \frac{X_0}{E_c/E_S}$, where $E_S = 21.2$ MeV is the scale energy [1].

Electromagnetic showers exhibit some attributes that make them relatively easy to measure. As λ_{photon} is almost the same as X_0, the longitudinal development does hardly depend on the initiating particle. The shower effectively consists only of electrons, positrons and photons, which means that almost all energy is used to ionize the detector material at the end. This results in a good correlation between measured energy fraction in the active layers and the energy of the incident particle.

Hadronic Showers

Hadronic showers are more complicated than electromagnetic showers. The strong interaction introduces some effects that complicate the energy measurement. In some processes energy is transferred to not measurable energy, like the nuclear binding energy in spallation processes or muons or neutrinos are created and leave the detector. The fraction of the invisible energy varies from event to event and degrades the energy resolution of a hadronic shower.

Another relevant feature of hadronic showers is, that they contain electromagnetic showers as well. These are produced via the creation of π_0 and η. These particle decay into two photons, from which electromagnetic showers are initiated. Again the fraction of π_0 and η varies from event to event.

The longitudinal development of a hadronic shower is described by the interaction length λ_{int}, the mean free path between two nuclear interactions. Like in the electromagnetic shower the number of particles increases till it reaches a maximum, which has a position depending on the energy, followed by a slow decrease of multiplicity. But since λ_{int} is larger than X_0, the amount of material necessary to contain a hadronic shower is much larger than for an electromagnetic shower of the same energy. The fluctuations in the shower distribution are also larger than for an electromagnetic shower.

Energy Resolution

Excluding effects like invisible energy fractions, the resolution of a sampling calorimeter is given by:

$$\sigma^2 = \sigma^2_{shower} + \sigma^2_{sampling} + \sigma^2_{calibration} + \sigma^2_{noise} \tag{1.1}$$

The nature of the different contributions leads to different behavior with energy. The number of particles created in a shower and the number of hit cells scale with energy. Both are discrete processes, such that a Poisson distribution is a proper description:

$$\sigma_{shower} = a_1 \cdot \sqrt{E}, \sigma_{sampling} = a_2 \cdot \sqrt{E}; \qquad a_1, a_2 = \text{const}$$

The error introduced by a limited precision of the calibration scales in the same way like the channel response and is in most of the cases linear with energy:

$$\sigma_{calibration} = b \cdot E$$

The electronic noise is a constant and does not depend on the signal measured:

$$\sigma_{noise} = c$$

Altogether the relative resolution can be written as the quadratical sum of the single distributions:

$$\frac{\sigma}{E} = \frac{a}{\sqrt{E}} \oplus b \oplus \frac{c}{E} \tag{1.2}$$

Hadronic showers show additional effects which broaden the distribution of the measured signal. The already mentioned fluctuations in not detected energy will add to the width. Another degradation effect comes from the fact that electrons, pions and protons do not automatically give the same response for example in scintillators. Thus the response function depends on the fraction of the different components in a hadron shower.

To eliminate the degradation by the different response to electromagnetic and hadronic showers two main approaches exist: hardware compensation and software compensation. Hardware compensation tries to equalize the response of the different kind of particles by an accurate choice of absorber material and the segmentation of the calorimeter. Software compensation tries to identify which signals are created by which component of the shower and equalizes the signals through weighting.

Whereas hardware compensation gives restrictions in the design of a calorimeter, software compensation depends much on the spacial resolution and such the ability to separate the different shower components in the calorimeter.

A new approach, which yet has to prove the applicability, measures simultaneously the relative fraction of the different showers in the calorimeter to improve the resolution.

1.2.2 Particle Flow and Jet Energy

In figure 1.2 the relative energy resolution is plotted versus energy for the calorimeters and the tracker[3]. The behavior corresponding to $\frac{1}{\sqrt{E}} + const$ for the calorimeters and the worse resolution of the hadronic calorimeter are visible.

For most of the occurring energies the tracker has the best energy resolution. Therefore, the tracker measurement should be preferred. But only charged particles can be measured by trackers, as neutrals do not ionize and leave tracks. The photons and neutral hadrons have to be measured by the calorimeters.

[3]In general the tracker measures momentum and not energy, for high relativistic particles in the limit $p \gg m_0 c^2$ the energy $E^2 = m_0^2 c^4 + \vec{p}^2$ becomes $E = p$

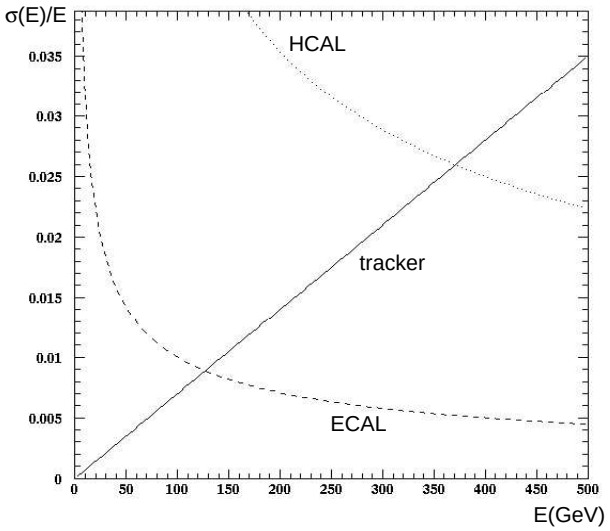

Figure 1.2: Energy resolution of different detector components [2].

When hadronic states are created in an event the typical signals are jets consisting of many particles and expanding in a quite narrow solid angle. The four-momentum of the primary partons are tightly correlated with the jet quantities. Thus the accuracy of the jet four-momentum measurement is directly related to capability to determine the partonic state.

Neglecting losses due the limited size of the detector and inefficiencies which will leave particles undetected the jet resolution is given by

$$\sigma^2_{jet} = \sigma^2_{\pm} + \sigma^2_{\gamma} + \sigma^2_{h^0} + \sigma^2_{confusion} \tag{1.3}$$

when charged and neutral particles are detected separately. The resolution of the energy measurement of charged particles $\sigma^2_{\pm}$ is preferably obtained by the tracker for most of the energies. The resolution of the electromagnetic calorimeter determines the photons resolution. Neutral hadrons will give signals in the hadronic calorimeter an thus are measured with its resolution $\sigma^2_{h^0}$. Finally, $\sigma^2_{confusion}$ expresses the fact that due to overlaps or inefficiencies of the particle flow algorithms the type of particle is misinterpreted, which will give additional uncertainties in the energy measurement.

When the signals of the neutral and charged particles are merged in the calorimeter, no profit can be taken from the good tracker energy measurement, as the calorimeter uncertainty is then on the full energy. When the energy can be measured separately for neutrals and charged particles in the calorimeter, only the part of energy transported by the neutrals contributes to the jet resolution.

To achieve a good separation of the neutral and charged particles a strong magnetic field and a very high granularity of the calorimeter are necessary. The magnetic field

separates neutral and charged particles. The high granularity is the basis to track the flow of the particles through the full detector.

1.3 CALICE

The CAlorimeter for the LInear Collider Experiment collaboration (CALICE) was founded to develop and test the calorimeter technology required by a linear collider.

The developments are driven by the aim of a detector exploiting the particle flow ansatz. This makes it especially important to consider the development of the calorimeters more as a system than simply optimizing the standalone performance of each device. Within CALICE prototypes of an electromagnetic and two hadronic calorimeters and of a tail-catcher and muon tracker are built. The combined performance of these prototypes will be tested in electron and hadron test-beams.

electromagnetic calorimeter (ECAL)
The electromagnetic calorimeter has a sandwich structure of tungsten absorber and silicon readout. The silicon is divided in pads of one square centimeter, which is the same order as the Molière radius of tungsten. In total it consists of 30 layers and ≈ 10000 channels (see [3]).

hadron calorimeter with analog readout (AHCAL)
A first hadronic calorimeter option tested by CALICE is a steel scintillator sandwich calorimeter. The scintillator is divided into tiles of 3×3 cm^2 smallest transversal size. Longitudinally the calorimeter consists of 38 active layers separated by 2 cm of steel. The scintillation light is read out with a newly developed silicon based photosensor (see [4]).

hadron calorimeter with digital readout (DHCAL)
The second study of a hadron calorimeter uses a different approach in the readout of the signal. The segmentation is increased further to cells of one square centimeter. No amplitude information is read from the cells, only the information of a hit above a fixed threshold is recorded. This motivates the name digital calorimeter. To reach this fine granularity ionization gas chambers are used with fine copper pad readout. Different amplification technologies are under study for this prototype: resistive plate chambers, gas electron multipliers and wire chambers.

tailcatcher and muon tracker (TCMT)
The calorimeter system is completed by a muon tracker with calorimetric capabilities. In the final detector it serves as a tailcatcher after the magnet. For the combined test-beam research of the system it serves as an extension of the hadronic calorimeter. It is built as iron scintillator sandwich like the AHCAL but with different scintillator geometry. One meter long and five centimeter wide strips with a central wavelength

shifting fiber are used and the signals are read by the same type of photodetector as the AHCAL.

test-beam data acquisition system
For the test-beam efforts a common data acquisition system is developed based on the VME[4] standard. A readout card hosting trigger logic, analog to digital conversion and steering of frontend settings is developed, the so called CALICE Readout Card (CRC) (see [5]).

For the subject of this text two detectors are of interest, the AHCAL and the TCMT. Both use a scintillator based readout. The light is measured with the same kind of photodetector making it possible to use the same readout electronics.

1.3.1 Analog Hadronic Calorimeter (AHCAL)

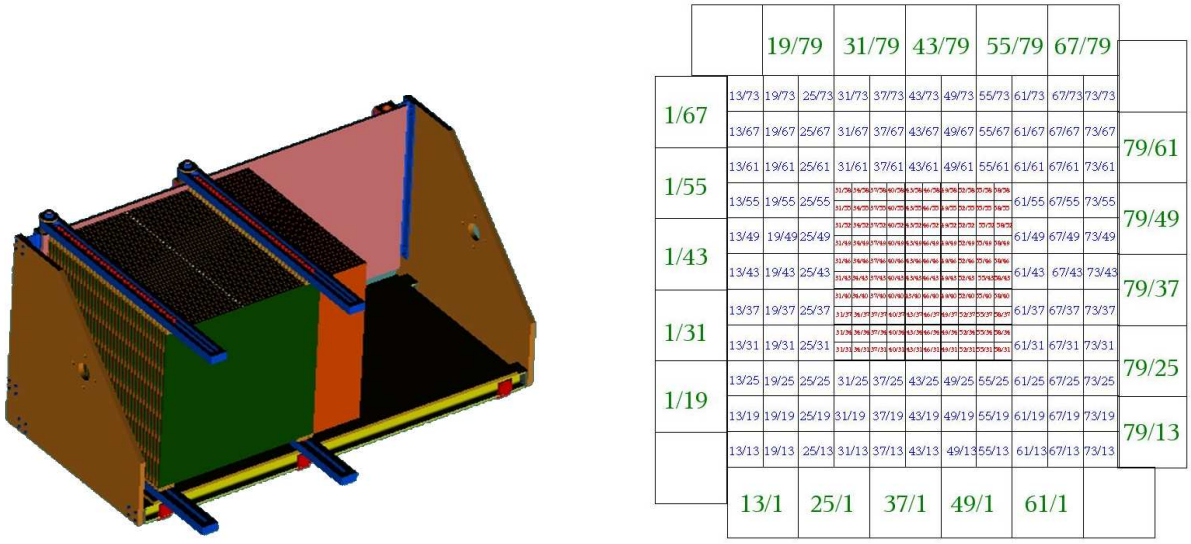

(a) AHCAL on support structure (model)

(b) AHCAL layer with fine core

Figure 1.3: Analog Hadronic CALorimeter (AHCAL)

The absorber structure of the hadronic calorimeter is build of steel plates 1 m^2 large and two centimeter thick. In figure 1.3(a) a model of AHCAL on its support structure is shown. The device has a cubic size of 1 m^3 volume and weighs approximately 8 tons.

The active layers are a mosaic of scintillator tiles. To save costs only the core uses the maximum segmentation of 3×3 cm^2. The fine core, which extends over the first 30 layers,

[4]Versa Module Europa is a standardized bus system for experimental electronics

is surrounded by an area of 6x6 cm^2 segmentation. The last 8 layers of the calorimeter have a homogeneous segmentation of 6×6 cm^2. To detect leakage a row of 12×12 cm^2 tiles encloses the inner calorimeter part. Figure 1.3(b) shows a sketch of such a scintillator mosaic with fine core.

The depth of one meter corresponds to $\approx 4.5\ \lambda$. A total of 7608 cells are read out individually. The mechanical structure allows to shift the layers with respect to each other to contain the shower in the highly granular core also when the beam is hitting the calorimeter center under an angle.

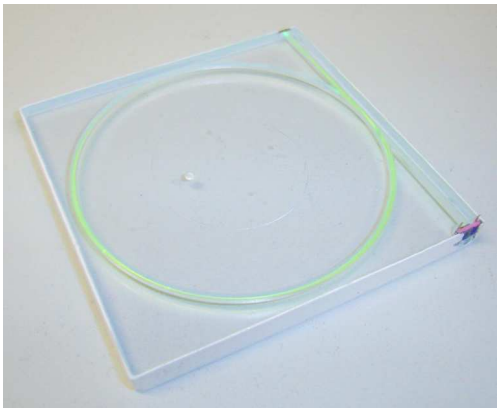

(a) AHCAL tile

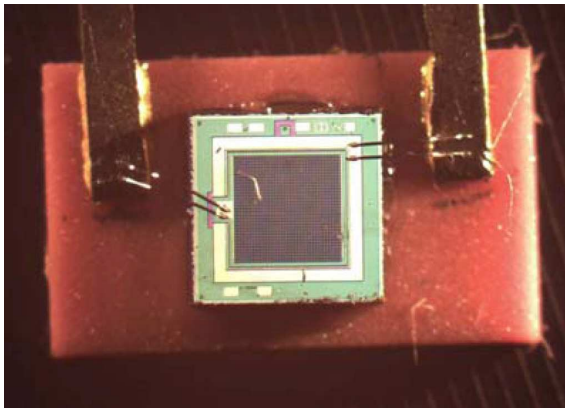

(b) SiPM

Figure 1.4: Particle detection in AHCAL with scintillator tiles and SiPM [6]

Figure 1.4(a) shows a single scintillator tile. The plastic scintillator has a groove in which a wavelength shifting fiber (WLS) is inserted. This fiber adapts the scintillation spectrum in the blue range to the green range where the photodetector is most sensitive. The photodetector is mounted at one end of the WLS in the tile.

The use of silicon photomultipliers (SiPM) as photon sensors has several advantages when building such a highly granular device. Three attributes, size, gain and sensitivity to magnetic fields, are important when the detector should be mounted into the calorimeter volume. SiPM have an active area of one square millimeter and the total size is not much bigger. In contrast to standard photomultipliers they are not sensitive to magnetic field and compared to APDs[5] the gain is high enough to transport the electric signal with over several decimeter to the amplifier. This avoids a complicated light transport system to detectors outside the volume. Figure 1.4(b) shows a picture of one of the used SiPM on its support. A detailed description of the SiPM follows in section 2.2.

[5]Avalache Photo Diode

1.3.2 TailCatcher and Muon Tracker (TCMT)

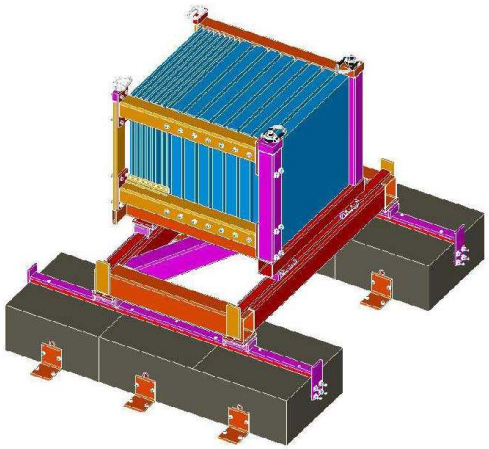

(a) TCMT absorber structure on moving system

(b) TCMT active layer design

Figure 1.5: TailCatcher and Muon Tracker (TCMT)

The tailcatcher and muon tracking system uses an absorber structure with two sampling frequencies. The first eight layers use 2 cm thick steel plates. The second half of 8 layers uses an absorber width of 10 cm. The total depth of the TCMT with readout planes is 1.4 m. The larger distance corresponds approximately to the spacing in muon system at the ILC. In the ILC detector the muon system is installed into the flux return of the magnet, leaving the coil between HCAL and TCMT uninstrumented. To have an insight into the processes happening in this part of a detector the resolution in the first eight layers of the prototype TCMT is enhanced to that of the AHCAL. The mechanical structure sitting on a rail system for later positioning is shown in figure 1.5(a).

The active planes of the tailcatcher are built of one meter long and five centimeter wide scintillating strips. These strips are produced by NICADD NIU[6]. A double strip, 10 cm wide, is extruded with two co-extruded holes for wavelength shifting fibers. The double strip is optically separated into two strips by a painted groove. SiPMs are used as photodetectors and are mounted on the end of the WLS fiber.

Figure 1.5(b) shows a drawing of a TCMT readout plane. As layer design gives only a one dimensional spacial resolution, subsequent planes are either x or y oriented.

[6]Northern Illinois Center for Accelerator and Detector Development at Northern Illinois University

Chapter 2

Readout Concept of the AHCAL and TCMT Prototypes

As already mentioned in section 1.3 the readout of the AHCAL and TCMT prototype can be established using the same electronics. The readout concept for these two devices is subject of this chapter. The text will mostly refer to the AHCAL, but unless specified otherwise it applies in the same way to the TCMT prototype.

2.1 Full Readout Chain

The process which creates a signal from a particle traversing a detector volume consists of a sequence of steps. These can be split into two parts, the processes happening in the combined scintillator photodetector system till an electrical signal is created and the amplification and registration of this electric signal.

2.1.1 The AHCAL Tile

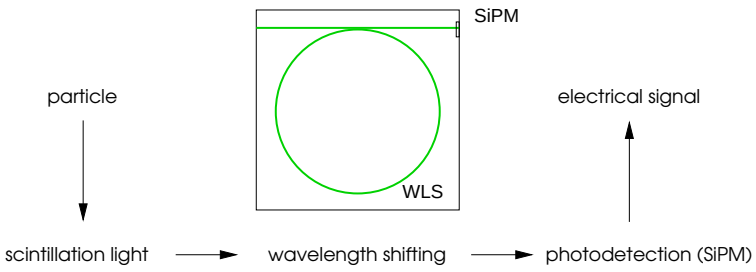

Figure 2.1: Particle detection in the AHCAL. Schematics of the processes in a single tile.

Figure 2.1 summarizes the signal chain in the scintillator system. When a charged particle crosses the scintillator plastics it deposits energy due to ionization. This deposited energy excites special added dopant molecules which then de-excite optically. The amount of produced light is proportional to the deposited energy. Industrially available plastic scintillator materials mostly use a combination of different dopants and radiate in the ultraviolet range.

The actual available silicon photomultipliers (SiPM) have a maximum sensitivity in the green range. For this, the detection efficiency can be increased by shifting the wavelength of the emitted UV photons to the green range. Wavelength shifting fibers absorb UV light by exciting molecular states which are de-excited in at least two steps, one non optical followed by an optical state at lower energy and thus longer wavelength. Such fibers are used to collect the scintillation light and guide it to the photodetector, the SiPM. This device translates the optical signal into an electrical signal. The detailed working principle is described in section 2.2.

2.1.2 The Electronic System

The total AHCAL prototype consists of almost 8000 channels. This implies some needs for the further processing of the electrical signal. To save costs and in the scope of a generalized readout for all prototypes it is not only practical to use standard analog to digital converters (ADC) but also to reduce the number of these devices and the cable connections. The way to reduce the necessary digitization channels is the application of multiplexing. This means that the signals from several channels are read successively on one ADC chip.

Another constraint for the electronic system is due to the use in a test-beam environment. The activation of trigger systems is initiated by the detected particles itself. Trigger calculation needs a certain amount of time and thus the analog signals have to be delayed as long as the activation of the readout system needs.

For the readout of the AHCAL and TCMT prototype an 18 channel Application Specific Integrated Circuit (ASIC) was designed which includes an amplifier, a shaper and multiplexing capability. In figure 2.2 the electrical signal processing is shown from the SiPM input signals to the multiplexed output signal. Each signal of the 18 connected SiPM (figure 2.2(a)) is amplified and shaped (figure 2.2(b)). The shaping is used to adjust the delay to the trigger needs and can be varied between approximately 50 ns and 180 ns. The maximum of the signals is held (figure 2.2(c)) and the 18 resulting signals are multiplexed to the single output line (figure 2.2(d)). A detailed description of the ASIC follows in section 2.3.

The ASIC output signal goes to the Data AcQuisition system (DAQ) to one ADC input. The DAQ system not only digitizes the analog signal, it also steers the frontend electronics and hosts the trigger logic. The main part of this system is the CALICE Readout Card (CRC) which hosts the dedicated electronics. Each card has inputs for 8 layers of the AHCAL and one trigger unit. A set of these cards, which are designed for the VME bus

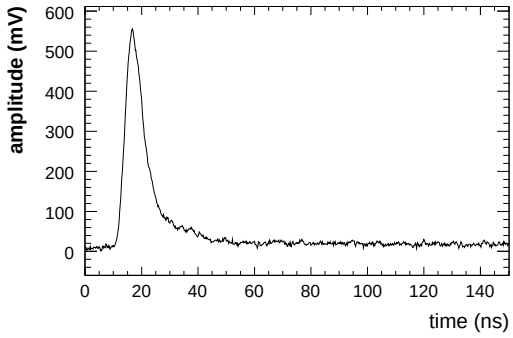

(a) SiPM signal (18×)

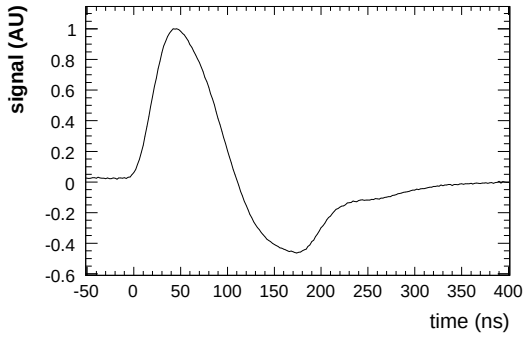

(b) Amplified and shaped signal (18×)

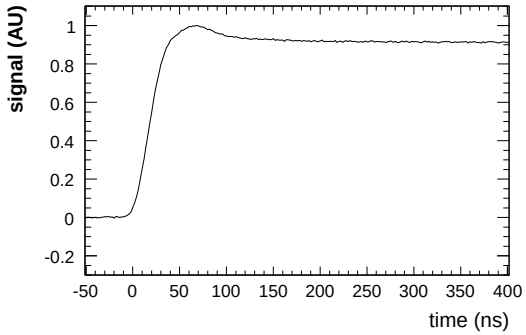

(c) Held signal (18×)

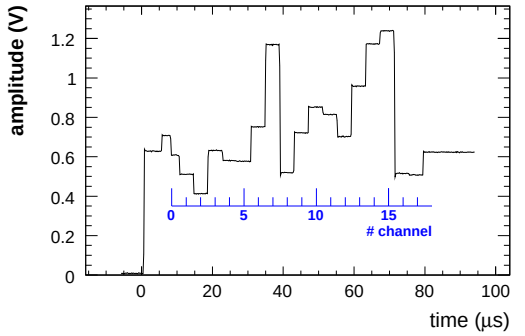

(d) Multiplexed signal (1×)

Figure 2.2: Electrical signal processing in the ASIC

system, make up the DAQ. The data is read over an optical link via the VME bus by a personal computer.

2.2 Photo Detection – SiPM

The scintillation light is detected with a newly developed device, the Silicon Photo Multiplier (SiPM). About 8000 pieces which are needed for the AHCAL and TCMT are produced by MEPHI[1]-PULSAR[2].

[1]Moscow Engineering and Physics Institute, Moscow, Russia
[2]"Pulsar Enterprise", Moscow, Russia

2.2.1 Structure and Signal Creation

The structure of a SiPM for CALICE is built by an array of 34×34 pixel covering a surface of $\approx 1\text{mm}^2$.

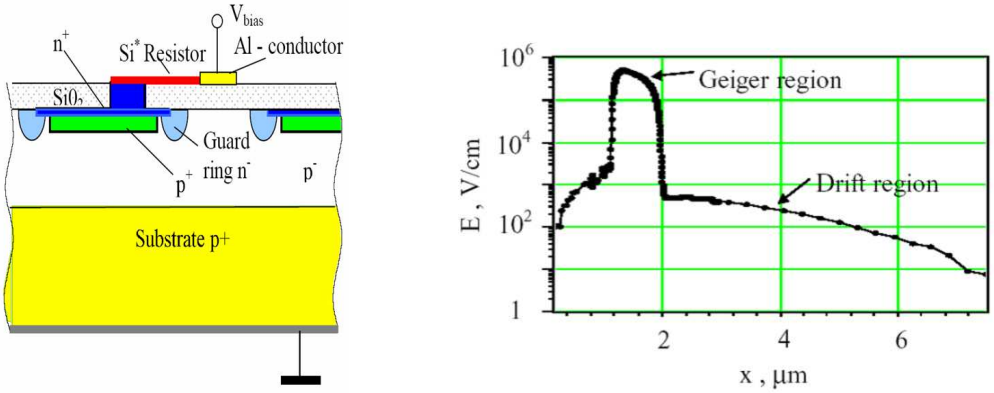

(a) Profile of a SiPM pixel

(b) Electric field in a SiPM pixel. X-axis is position from top to bottom.

Figure 2.3: Schematic picture of a SiPM pixel and the resulting electric field [7]

Figure 2.3(a) shows the semiconductor structure of a single pixel. Each pixel works like an avalanche photo diode (APD) in Geiger mode. If an electron is created in the drift region of a pixel it will move into the multiplication region due to the electrical field. The electron gains enough energy to create secondary electrons by ionizing the silicon, through the very high electric field in this part of the pixel. The charge carriers created in this ionization process, electrons and holes, are themselves accelerated enough to ionize the silicon. The result is an avalanche like multiplication of the charge carriers in the pixel volume.

The avalanche created in this way has to be quenched, otherwise it would continue for a long and hardly predictable time. For this device the quenching is performed passively with a high ohmic resistor ($1 - 20$ MΩ) in the bias circuit of each pixel. If the current increases, the voltage drop over the resistor will reduce the bias voltage so far that the avalanche is stopped. The large resistor is also necessary to electrically decouple the pixels from each other.

The amount of charge released when a pixel is fired is defined by the geometry and operation parameters of the pixel and not by the initial charge created by a photon. The charge Q depends on the overvoltage ΔV, $Q = C \cdot \Delta V$, $\Delta V = V_{bias} - V_{breakdown}$, where $C \approx 50$ fF is the pixel capacitance.

The signal shape of a firing pixel is shown in figure 2.4(a). It shows a very steep rise (less than 500 ps) caused by the fast increase of charge carriers (electron and holes)

moving in the pixel volume. At a certain point, when the electrical field is no longer strong enough for multiplication, the free charge will decrease by recombination of electrons and holes and by charge carriers leaving the pixel volume over the circuitry. This leads to a fast part followed by a slow part of the falling signal. The high space charge from the created electrons destroys the electrical field as shown in figure 2.3(b), therefore a detailed description of the quench process is not possible with a simple model.

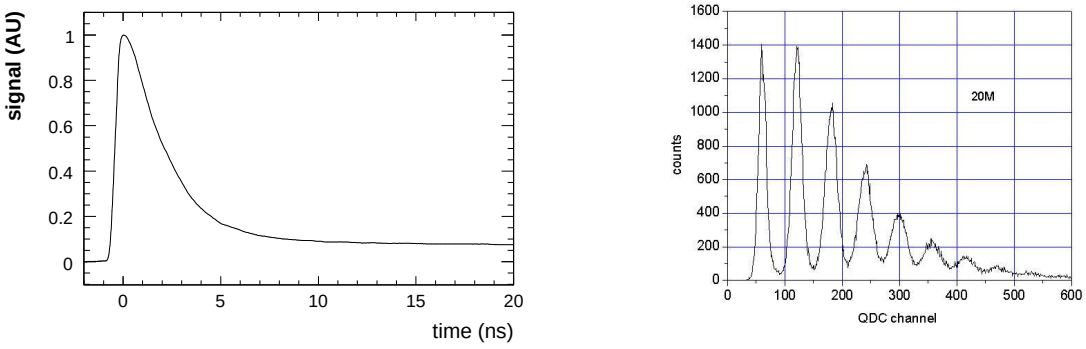

(a) SiPM single pixel signal (drawing)

(b) SiPM signal charge spectrum for low light intensity for 20 MΩ quenching resistor SiPM [8]

Figure 2.4: SiPM signal and signal spectrum

A general dependence is kept between the resistor and the time it needs till the electrical field is restored in a pixel. The larger the resistor the longer the recovery will be. This allows the production of SIPM with a pixel recovery time much larger than the photon signal duration, which leads to an output signal charge independent of the input signal time distribution.

The necessity to create very high electrical fields in a small space leads to quite some variations in the working parameters of SiPM even in one series. For example the break-down voltage varies from device to device. This makes it necessary to tune every SiPM to its optimal working point and therefore to have an individual supply of the bias voltage.

The full device has to be seen as parallel circuit of 1156 current sources, each responding individually to photons. The signals of the individual pixels add and from the charge the number of fired pixels follows directly. As every photon hitting the device has a certain probability to fire a pixel the number of fired pixels follows the number of incident photons.

The detection efficiency of a SiPM $\eta_{tot} = \eta_{QE} \cdot \eta_{geo} \cdot \eta_{Geiger} \approx 10 - 17\%$ is the product of quantum efficiency ($\eta_{QE} \approx 80\%$), geometrical efficiency ($\eta_{geo} \approx 20 - 35\%$) and Geiger efficiency ($\eta_{Geiger} \approx 60\%$) [7] [9].

The total signal charge can be expressed as $Q_{tot} = N \cdot Q_{pixel}$ where N is the number of fired pixels. Therefore, the output spectrum of the SiPM consists of discrete amounts

of charge. Figure 2.4(b) shows a typical signal spectrum of SiPM, when illuminated with LED light of a small flux, corresponding to a few detected photons. The spectrum was measured with a charge sensitive ADC[3]. The distance between adjacent peaks corresponds to the charge per pixel which is the gain of the device under the assumption that a pixel is fired by one photoelectron. The finite geometrical precision of production leads to a random distribution of single pixel gains. Together with the fluctuations in the avalanche process this determines the single pixel signal width.

In general it is very helpful to use the signal of single photoelectrons to obtain an absolute calibration of a detector. In the SiPM case this is especially true, as the relation between signal and signal width does not follow $\frac{A}{\sigma} = \frac{N}{\sqrt{N}}$.

At low amplitudes, the relation between signal and signal width is affected by optical crosstalk between single pixels. Photons are created with a probability in the order of 10^{-5} during the avalanche process. As the amplification is in the order of 10^5 - 10^6 each fired pixel is the source of a few photons which may fire another pixel. The probability for this process is roughly 30% at very low light fluxes. But it will decrease with the amount of fired pixels, as the photons created in this process will hit already fired pixels with increasing probability.

At hight amplitudes, the maximum SiPM signal is limited by the finite number of pixels. In consequence, the response function of the SiPM is not linear. The actual response function of the SiPM-scintillator system depends on the SiPM gain and the light-yield of the scintillator-SiPM-system. For the measurement and correction of the SiPM response it is essential to resolve single photoelectron spectra (see also [10]).

2.2.2 Signal Dependencies

As the SiPM is a semiconductor it shows a large temperature dependence. Due to an increase of the phonon density with temperature the mean free path of electrons in a semiconductor decreases with increasing temperature. A smaller mean free path gives a higher probability for electrons to loose a fraction of their energy before they can ionize the silicon. This effect increases the breakdown voltage with temperature. In our case, the bias voltage will stay the same, resulting in an reduction of the gain G with increasing temperature. For our kind of SiPM a reduction of $\frac{\mathrm{d}G}{\mathrm{d}T} = -1.7\frac{\%}{\mathrm{K}}$ was quoted by the producer [9]. But not only the gain is affected by the temperature, also the detection efficiency changes with temperature. Accordingly, the total response, which is the product of gain and efficiency, changes according to $\frac{\mathrm{d}A}{\mathrm{d}T} = -4.5\frac{\%}{\mathrm{K}}$ [9].

The amplification mechanism of the SiPM, as described in section 2.2, is based on avalanches created in a high electrical field. As a result of this, gain and total response depend strongly on the bias voltage: $\frac{\mathrm{d}G}{\mathrm{d}V} = +2.5\frac{\%}{0.1\mathrm{V}}$, $\frac{\mathrm{d}A}{\mathrm{d}V} = +7\frac{\%}{0.1\mathrm{V}}$ [9].

In addition to the effects caused by the material properties, there are some effects caused by the limited number of pixels. The recovery time of the pixels is much longer

[3]ADC: analog to digital converter, converts in this case charge to a digital value.

than the average signal duration. This means, that every pixel can fire only once during one event. At first this leads to a nonlinear response of the SiPM to the input signal due to saturation. But it influences the signal shape in addition.

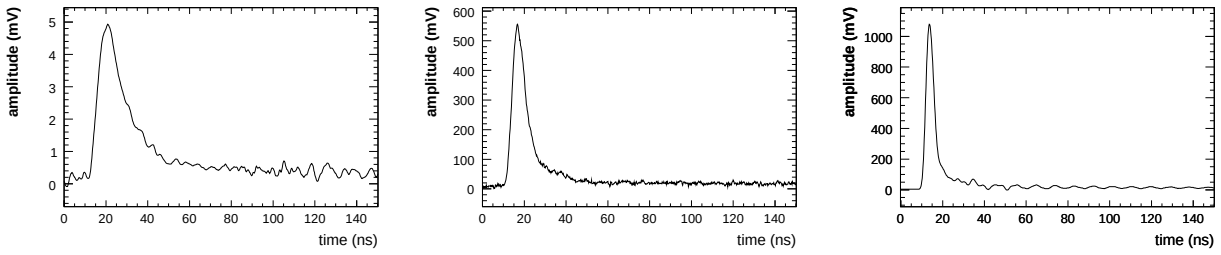

(a) (b) (c)

Figure 2.5: Shortening of SiPM signal with increasing amplitude from (a) to (c)

If the light pulse measured by the SiPM is very short, shorter than the pixel signal, the output signal shape is determined by the pixel signal shape and independent of the photon flux of the source. If the light signal duration is longer than the response of a pixel, the output signal width will show the timing of the light signals, at least for signals with low amplitude. If the amount of fired pixels is large enough to show saturation effects, this will also have an influence on the signal shape. To understand this one can think of a case where the amount of light coming from a source with a decay time τ is firing all pixels of a SiPM. If the light is increased the total charge will not change, as there are no more pixels that can fire. But as the number of photons which is needed to fire all pixels is reached faster the signal of the SiPM will shorten. In the extreme it will be again of the single pixel shape. This effect can be seen in figure 2.5, where for low amplitudes (a) the signal maximum is around 25 ns, while the full fast signal part is within 20 ns for high amplitudes (c). Depending on the used readout electronics this may or may not be an issue.

A third effect of the limited number of pixels is the already described reduction of the crosstalk with signal amplitude.

2.2.3 Noise

The SiPM will be operated at room temperature. For semiconductor devices, especially if operated at such high gains, this results in a significant dark rate. Measurements of the CALICE SiPM show pulses of one pixel or more with a frequency of 1-3 MHz. The rate reduces to 1 kHz at half the signal level of a MIP. This high rate can lead to a bias of the

signal depending on the integration time of the electronics. In addition this may fake some MIP events in cells where no particle has hit.

As the SiPM shows single pixel resolution and a MIP fires on average 15 pixels for our scintillator SiPM system, the resolution of MIP signals will be dominated by the statistical fluctuations of the detected photons.

2.3 Signal Amplification – ASIC

For the amplification of the SiPM signal before digitization an application specific integrated circuit (ASIC) was developed by LAL[4]. The design of this chip is a derivative of the ECAL chip which was already present. This choice has several advantages, as it is easy to use the same DAQ for both ECAL and HCAL. To start a development with the knowledge already gained by the ECAL design leads not only to a decrease of the costs but to an increase in production quality and efficiency.

The approach for the design of this chip is to process and multiplex the analog signals before these are digitized. This analog design has advantages in power consumption and heat development but the information about the signal shape is lost. A readout study, that uses a fast digitization of each channel and integrates the SiPM signals offline, is under development in parallel. This will give a better understanding of both methods, especially as the SiPM signal shape varies between production series and with amplitude. This thesis will concentrate on the analog chip used in the test-beam readout.

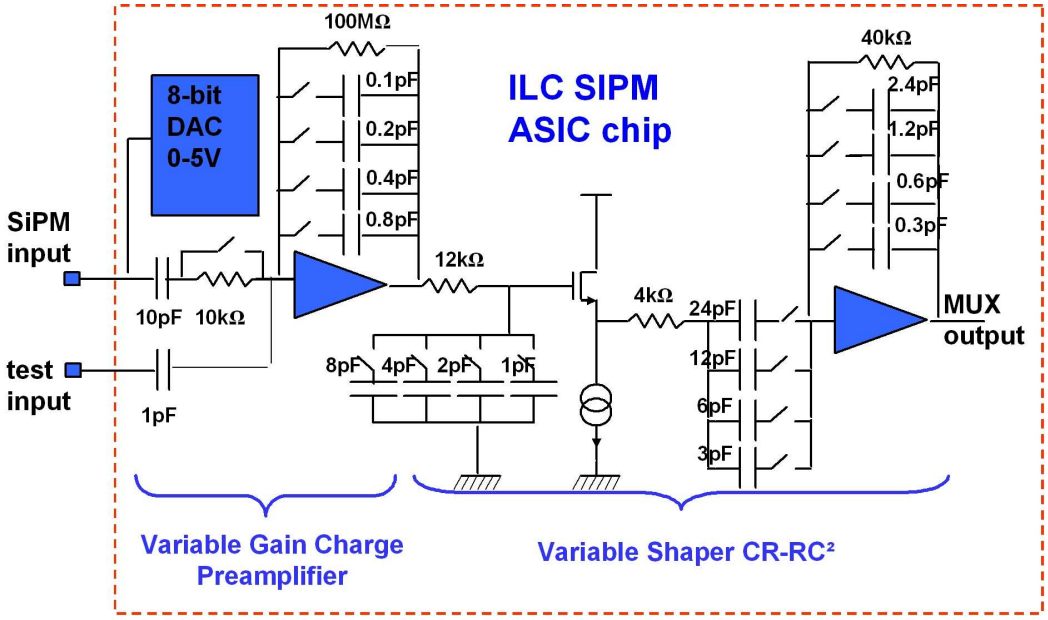

Figure 2.6: ASIC chip schematics [11]

[4]Laboratoire de l'Accél'erateur Lin'eaire, IN2P3-CNRS - Université Paris-Sud

2.3.1 Schematics and Response

Figure 2.6 shows the layout of the LAL ASIC. The value of interest for SiPM is charge as shown in 2.2.1. Therefore, a charge sensitive amplifier is a natural choice. One standard way of realizing such an amplifier is a capacitive feedback over a voltage amplification stage, shown in figure 2.7(a).

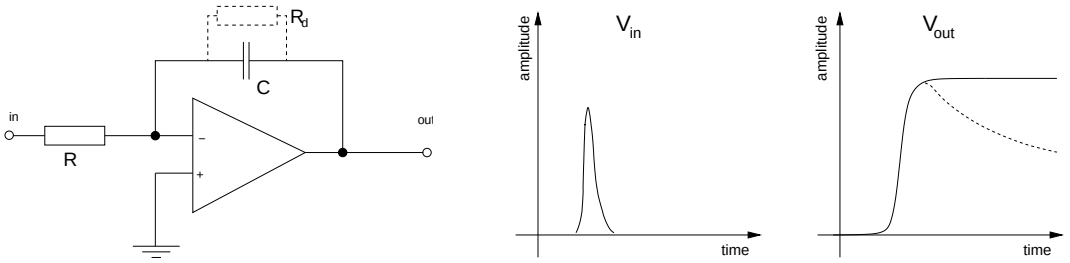

(a) Charge integrating amplifier circuit

(b) Response of a charge integrating amplifier to a signal pulse

Figure 2.7: Charge integrating amplifier circuit and response. The dotted lines show how the integrated charge is removed passively in this circuit.

The operation amplifier, pictured as a triangle, can be idealized as a device amplifying the difference between the inverted $(-)$ and non-inverted $(+)$ input $V_{out} = A \cdot (V_+ - V_-)$ with infinite gain A. Using a feedback loop the output voltage will regulate the input voltage difference to zero. When the positive input is grounded as in the example circuit, the negative input will be also at zero volts generating a virtual ground. The virtual ground together with the idealization, that no current flows into the operation amplifier input itself, allows an easy description of the working principle of such an amplifier.

The signal charge coming from the detector flows over the resistor R to the virtual ground. As the operation amplifier does not draw any current, the current has to flow over the feedback loop and charges up the capacitor. This leads to the voltage

$$V_{out} = -\frac{Q}{C} \tag{2.1}$$

at the voltage amplifier output. The total gain

$$G = \frac{V_{out}}{Q} = -\frac{1}{C} \tag{2.2}$$

of this circuit, relating the input charge to the output voltage, depends only on the value of the capacitor assuming an ideal operation amplifier. In the ASIC design the value of the feedback capacitance, and thus of the gain, can be varied by enabling or disabling up to four different capacitors.

The charge accumulated on the capacitance has to be removed to not pile up more and more signals. In this circuit this is done passively by a resistor. Figure 2.7 shows the circuit and signals with and without this resistor. The time constant $\tau = R \cdot C$ for the discharge is chosen large compared to the signal duration and varies between 10μs and 150μs, depending on the chosen gain.

The amplification stage is followed by an RC-CR^2 shaper, with variable shaping times. One of the main reasons for a shaper in signal processing is the reduction of the bandwidth, which can be used to improve the signal to noise ratio of an amplifier. Another motivation for the use of signal shaping is the predictable timing of the output signal.

The large amount of channels makes it reasonable to use multiplexing (see also 2.1.2). This reduces the complexity for cabling and cost for digitization electronics. But it creates the need to save the signals as well. Each of the amplifier chips has 18 inputs which are amplified and shaped in parallel. With an external hold signal the momentary amplitudes of the channels can be saved to capacitors (see 2.2(c)). This analog signals can be switched successively to the single output line to be read by an ADC (see 2.2(d)). The fact, that this hold signal has to be applied externally, determines the shaping time in a test-beam setup, which should be slightly greater than the maximum time needed to calculate the hold signal from the trigger.

Like the gain, the shaping time can be varied in 16 steps, ranging from 12ns to 180ns. The response of such a shaper is given for a step function like input signal by

$$V(t) = V_0 \left[\frac{t}{\tau} - \frac{1}{2} \left(\frac{t}{\tau} \right)^2 \right] e^{-\frac{t}{\tau}}. \tag{2.3}$$

Comparing the duration of the SiPM signals to the time constant of the shaper the step function approximation is not fulfilled. This leads to a later occurrence of the output maximum. Furthermore, the SiPMs show different ratios between the fast signal part and the tail depending on the production series. For a homogenous timing only SiPM of same ratio should be used in one module.

To measure the SiPM gain the electronics has to be able to resolve single pixel signals. To achieve a good separation of the peaks the gain has to be high and the noise small. In addition the integration time has to be small enough to minimize signals from dark rate, which pile up to the signal.

Such a mode is realized by not only choosing the smallest shaping and highest gain of the ASIC but also bridging the 10 kΩ input resistor of the amplifier circuit. This changes the characteristics of the amplifier stage. The charge is not anymore integrated on the capacitance, it will flow back over the decoupling capacitor and the termination circuit to the ground (see figure 2.8). The dependency between input signal and output signal becomes more complicated and it will depend on the input signal shape. It is possible to simulate the exact behavior numerically, but an idealized description is not anymore possible.

The large variety of operation modes offered by the ASIC chip gives the opportunity to amplify more than only SiPM signals with the same chip design. This is a big advantage as signals from monitoring devices like PIN-diodes (see [10]) or photomultipliers can be read out over the same chain with not much additional electronics.

2.3.2 Individual SiPM HV Adjustment Using a DAC

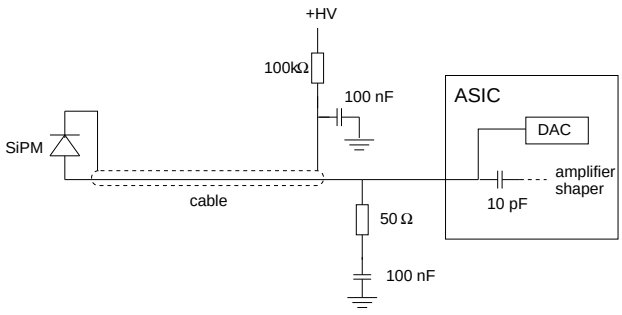

Figure 2.8: SiPM connection scheme

The SiPM operation voltage may vary from device to device, as already mentioned in section 2.2.1. Therefore, the electronics has to be able to individually tune the bias voltage for each channel. The ASIC chip has for each input channel an integrated 8 bit digital to analog converter (DAC) with a range from 0 - 5 V, giving a step resolution of 0.02 V. The connecting scheme in figure 2.8 shows how this voltage is used to reduce a common positive bias voltage. Without this feature each channel would need its own high voltage power supply, resulting in very high costs and for sure fragile cabling. On the other hand, this method's accuracy depends on the quality of the DAC and there is no monitoring of current or voltage for single channels available.

2.3.3 Very Front End Board (HAB) and Mother Board (HBAB)

Each ASIC chip sits on a small PCB board, which hosts electronics to supply the operating power and steer the settings of gain, shaping and DAC. Figure 2.9(a) shows a picture of this board. The steering of the ASIC settings is done with shift registers (SR). These are programmed over two lines, clock and data. The bits move one position forward for every clock cycle. The output of the SR of one VFE-board is connected to the input of the next. Every six boards build a serial line of SR which are programmed by the data acquisition (DAQ). The output of the last board is read back for verification by the DAQ.

As the voltage settings of the DAC will be set only at the startup and stay the same for the time of operation, the programming of the settings is done separately for DAC and the remaining settings. To distinguish between these two programming modes the SR clock signal is switched by an external signal (SW_DAC) between both sets of SR. At

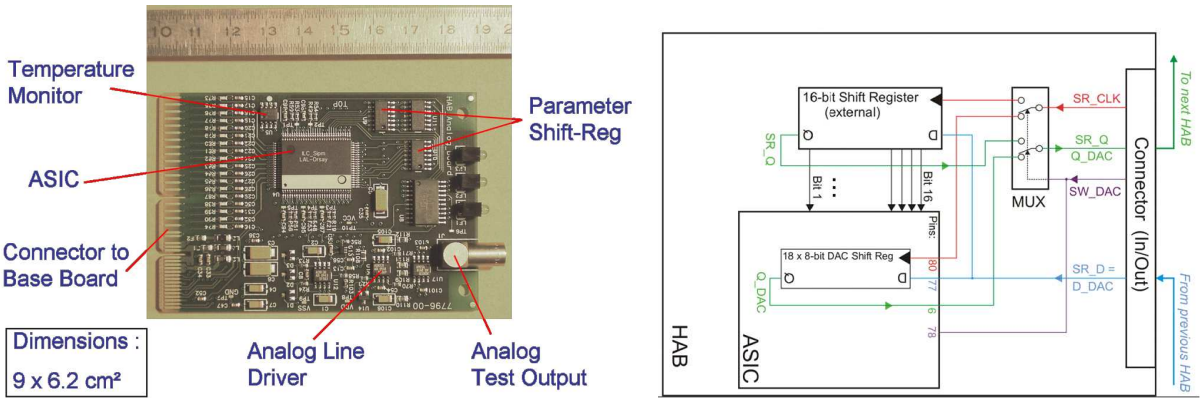

(a) Picture of the very front end board called HCAL Analog Board (HAB)

(b) Steering logic of the shift register

Figure 2.9: HCAL very front end electronics (VFE) [12] & [13]

the same time the output is switched to the right path to preserve the chain. A detailed scheme of the steering logic can be seen in figure 2.9(b). The separation of the two paths has two main advantages. On the one hand, the time used for programming the gain and shaping settings is reduced with respect to one single SR line. On the other hand the SiPM are constantly powered as the voltage settings are kept as long as the DAC is not reprogrammed. In addition the DAC SR is less sensitive to external noise as the clock line is disconnected during normal operation. This reduces the risk of applying a wrong voltage to the SiPM.

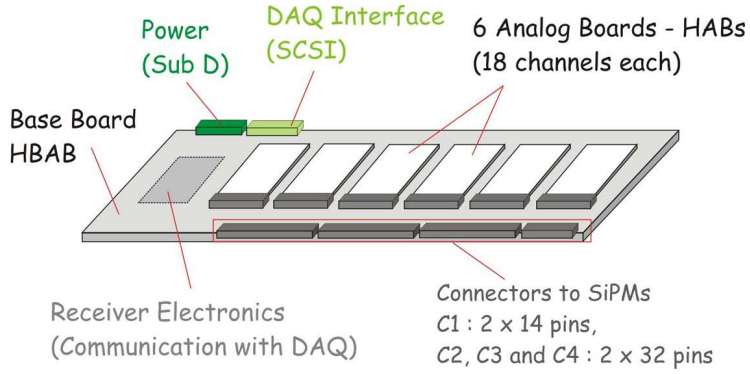

Figure 2.10: Drawing of the mother board type A hosting six very front-end boards [13]

The very front-end boards are connected over a mother board to the SiPMs and the data acquisition. The mother board also serves for the distribution of the low and high voltage supply. For size reasons the readout of one AHCAL plane has to be done by two

mother boards. This results in two mirrored versions of the mother board, type A and B. Figure 2.10 shows a drawing of an A-type motherboard.

Six very front-end boards sit on each motherboard, resulting in 108 input channels and 6 output lines. As there is one high voltage supply to a mother board, the SiPM connected to it have to lie within the range of the ASIC DAC. The six boards build one SR chain. The cabling of the SiPM in the AHCAL can be seen in figure 2.11 showing an open module equipped with electronics.

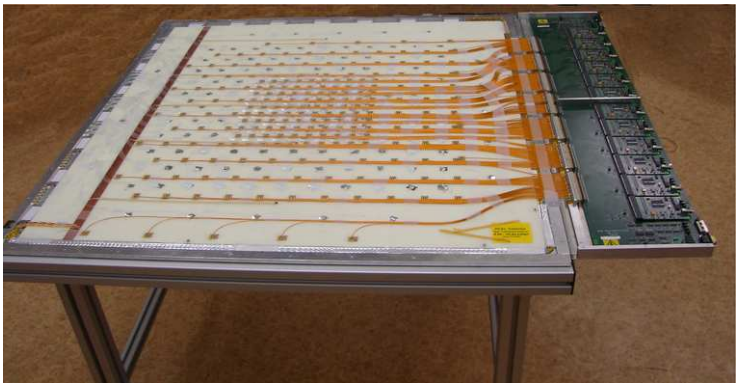

Figure 2.11: Picture of an opened AHCAL module with readout electronics.

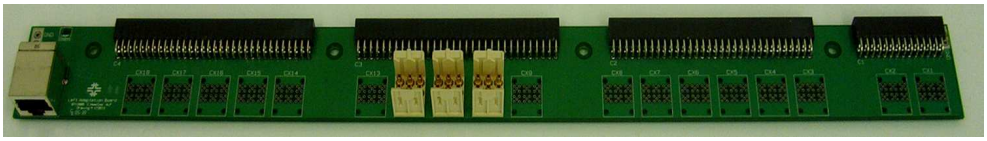

Figure 2.12: Picture of a prototype TCMT adaptor board.

The design of the very frontend electronics is optimized for the AHCAL modules with fine core. The TCMT has only 20 channels per layer, so that 5 modules can be joined on one mother board. The connection is realized using an adaptor board, which is shown in figure 2.12, and coax-cables.

2.4 Data Acquisition and Processing

For the later analysis the analog signals have to be recorded. But not only the pure amplitude in each channel has to be known to get meaningful information. As described in section 2.2, the SiPMs have a nonlinear response and are sensitive to temperature changes and operation parameters. A dedicated calibration and monitoring system is integrated into the AHCAL prototype and has to be steered by the data acquisition (see [10]). In addition to a measurement of the temperature with sensors integrated in the prototype, the operation parameters like high voltage including the ASIC DAC settings have to be

known. The ASIC will be operated in different gain modes which makes it necessary to record the applied settings. And last but not least a test-beam environment will have several kind of triggers like beam particle, calibration, pedestal or cosmics which should be separable.

2.4.1 CALICE Readout Card (CRC)

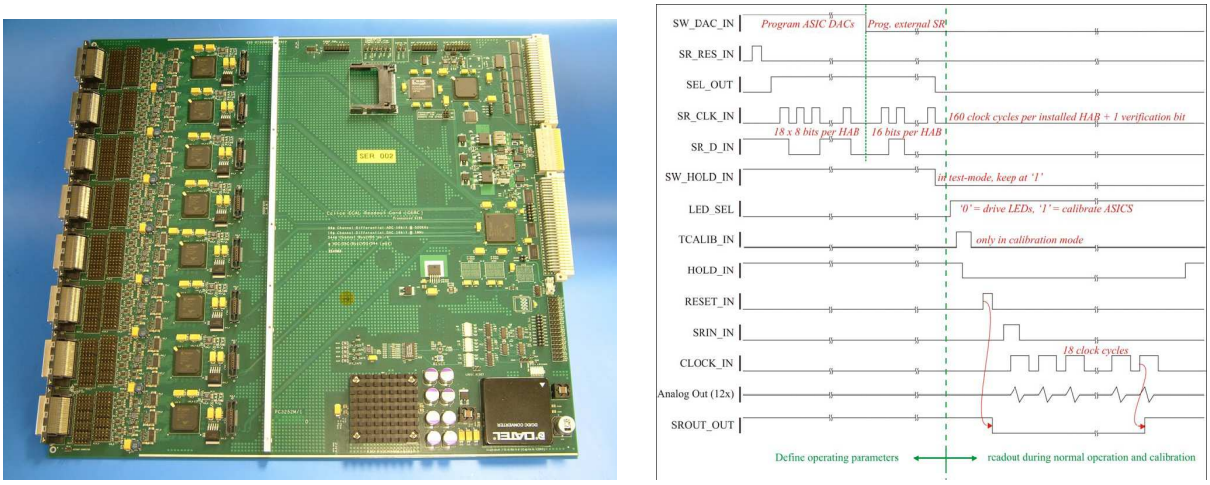

(a) CALICE Readout Card

(b) Programming and readout sequence

Figure 2.13: CALICE Readout Card [14] and readout sequence [13]

The heart of the data acquisition is formed by the CALICE Readout Card which is shown in figure 2.13(a). It can be split in two functional parts, the front-end (left of the separator) and the backend (on the right). The backend hosts electronics for the trigger detection and distribution. The readout sequence can be started by an external signal or an internal clock. The processing time needed for a trigger decision in this part is the greatest contribution to the trigger latency.

A frontend consists of inputs to the analog to digital converters (ADC) and outputs for the steering of the very frontend electronics. Figure 2.13(b) shows the signal sequences for the shift register programming and the readout of the multiplexed signals.

The CRC is capable of two different readout modes. One mode runs continuously and every event is read out directly by the DAQ software. In this mode the trigger speed is limited to the speed of the data transfer over the VME bus which is in the order of 100 Hz. As many test-beams do not deliver particles continuously, the DAQ can run in a buffering mode where up to 2000 events can be stored in the memory of the CRC and will be read in between two beam spills. This increases the maximum trigger rate to $\approx$ 1kHz and thus the efficiency at test-beams with non continuous beam supply.

Chapter 3

Characterization Measurements

The calorimeter energy resolution, equation 1.2, is affected by the readout electronics. Systematic effects in the readout system like saturation behavior would directly contribute to the constant term of the resolution and degrade the calorimeter performance at high energies. The influence of the electronic noise increases with decreasing energy.

Several measurements were performed to get a detailed understanding of the readout electronics, to avoid or at least understand systematic behaviors and its limitations. In addition the noise was measured for all parts of the electronics to be sure that no critical noise in addition to the unavoidable preamplifier noise is introduced.

In the following, measuring a value means recording the distribution of the signal with help of computerized systems for one set of operation parameters. A Gaussian distribution

$$f(x) = \frac{1}{\sqrt{2\pi}\sigma} \cdot e^{-\frac{(x-\mu)^2}{2\sigma^2}} \tag{3.1}$$

of the signal is assumed, as long as not noted differently. The errors on measured or derived parameters are called δ to avoid confusion with the standard deviation σ of the Gaussian distribution. For a Gaussian distribution the resulting errors are

$$\delta_\mu = \frac{\sigma}{\sqrt{N-1}} \tag{3.2}$$

$$\delta_\sigma = \frac{\sigma}{\sqrt{2N-1}}. \tag{3.3}$$

where N is the number of measurements, μ the mean of the Gaussian distribution.

The nature of the Gaussian distribution, where $\mu =< x >$ and $\sigma =$ RMS, gives the possibility to retrieve these values without actually performing a fit. This principle was used where applicable.

3.1 ASIC

The measurements performed mainly in two modes. One mode, called calibration mode, is used to resolve the single photoelectron peaks. The feedback gain setting for this mode is 0.1 pF, corresponding to the largest possible amplification. The input resistor is bridged and the fastest shaping time of 12 ns is used. The second mode, referred to as physics mode, uses the longest shaping of 180 ns, the 10 kΩ input resistor and a gain setting of 0.5 pF (see 2.3).

3.1.1 Gain and Linearity

The gain of an amplifier is not stable for all types of input signals. This could for example be the result of a limited input bandwidth or saturation effects for large signals. The linearity of the gain with amplitude is especially important in our case, as the full understanding of the SiPM nonlinearity is part of the studies.

Pulse Signals – Amplitude Response

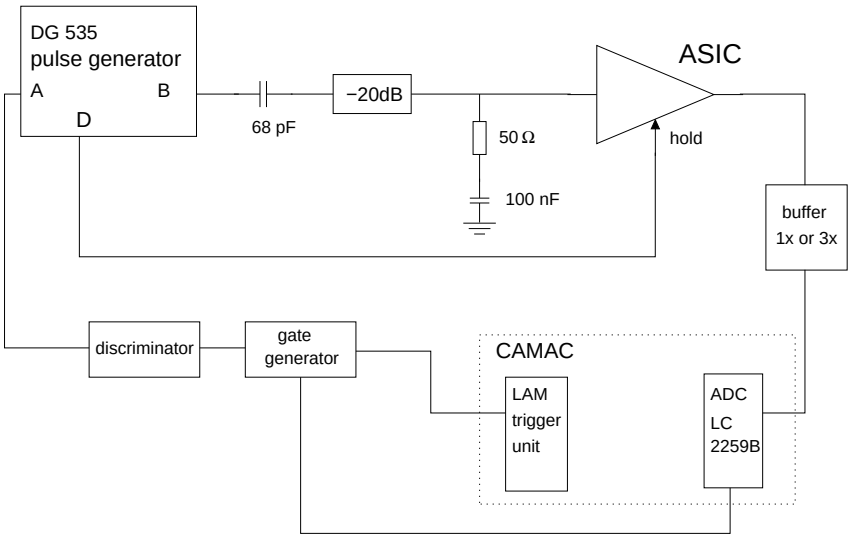

Figure 3.1: Setup to measure the linearity of the ASIC with injected charge pulses

A setup based on CAMAC[1] readout was built to measure the linearity of the ASIC gain. The gain is defined as the output voltage divided by the input charge.

$$G = \frac{V_{out}}{Q_{in}} \qquad \left[\frac{\mathrm{mV}}{\mathrm{pC}}\right] \tag{3.4}$$

[1] Computer Automated Measurement And Control

To create a short pulse of known charge a small capacitor $C = 68$ pF is charged up by a step function pulse from a pulse generator. The charge resulting is $Q_{in} = C \cdot V_{in}$. Like in the final setup, the cable used to inject the charge has an impedance of 50 Ω. This gives a time constant of $\tau = R \cdot C =$ 3.4 ns for the resulting pulse. For the measurement of the ASIC mode with the highest gain an attenuator of −20 dB was used to decrease the signal to one tenth. The so called physics mode was measured without this attenuator. The same pulse generator sends also the signals for the ASIC hold, the gate and the trigger for the CAMAC readout.

The output signal of the ASIC is measured with an LeCroy 2259B 11bit ADC ranging from 0 to 2 V. The linearity of this was checked with a voltage source controlled by a KEITHLEY 2001 multimeter. The accuracy of this device is 1 μV or better. The relation between input voltage V_{in} and ADC channels is $A = (0.9570 \pm 0.0003)\ \frac{\text{chan}}{\text{mV}} \cdot V_{in} - (0.7284 \pm 0.0006)$ chan. The maximum error due to nonlinearity of the ADC is one channel in the range of the measurement. For each point the mean was measured with a statistic of at least 10000 entries. The width σ_{gauss} of the resulting Gaussian was equal or smaller than 3.0 channels. This defines the error of a measured point as

$$\delta_A = \sqrt{\left(\frac{\sigma_{gauss}}{\sqrt{N-1}}\right)^2 + \delta^2_{linearity}} \approx 1 \text{ [chan]}. \tag{3.5}$$

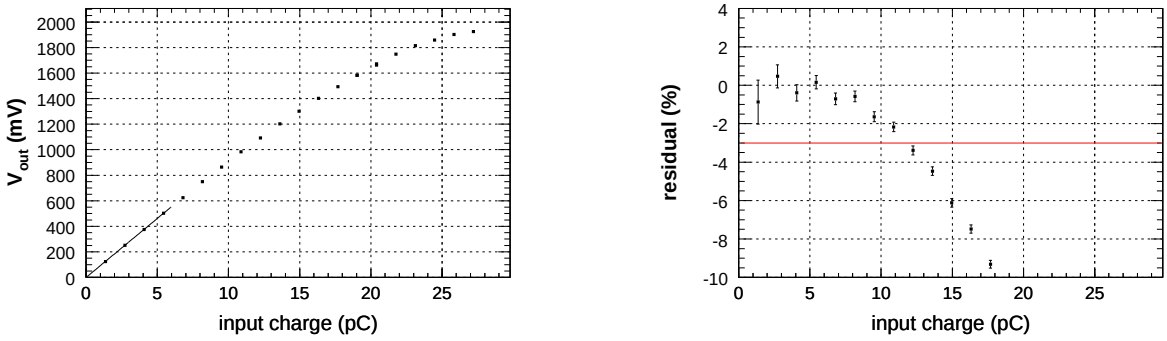

(a) ASIC response function

(b) Residual of the response function to linear fit

Figure 3.2: Calibration mode linearity

Figure 3.2(a) shows the response function of the ASIC in the calibration mode. The measured values are pedestal subtracted, $y = A_i - A_0$ and $\delta_y = \sqrt{2} \cdot \delta_A$. The statistical error on the x-axis is given by the precision of the pulse generator $\delta_{V_{in}} \approx 0.009$ mV

$$\delta_x = x \cdot \frac{\delta_{V_{in}}}{V_{in}}. \tag{3.6}$$

The accuracy of the capacitor adds a 10% systematical error on the x-axis. For the linear range and the gain this uncertainty is applies analogous. In the results only the statistical error is quoted.

The gain of the amplifier is measured for low amplitudes by fitting the first part of the curve. The range must not be chosen too big, as the nonlinearity at higher values would bias the result. For the fit a line through the origin was used $y = G \cdot x$. The gain determined in this way is: $G = (92.3 \pm 0.2)\ \frac{\mathrm{mV}}{\mathrm{pC}}$.

The deviation $y_{res} = \left(\frac{y}{G \cdot x} - 1\right) \cdot 100\%$ of the measured points to the fit of the first 4 points is plotted in figure 3.2(b). Here the limited range of constant amplification can be seen easily. If one accepts a maximum deviation of 3% the range reaches up to 11.5 pC in this mode. The error for the y-axis is given by

$$\delta_{y_{res}} = \frac{y}{G \cdot x} \cdot \sqrt{\left(\frac{\delta_y}{y}\right)^2 + \left(\frac{\delta_x}{x}\right)^2 + \left(\frac{\delta_G}{G}\right)^2} \cdot 100\%. \tag{3.7}$$

Figures 3.3(a) and 3.3(b) show the same measurement for the physics mode. The gain found is $(8.178 \pm 0.007)\ \frac{\mathrm{mV}}{\mathrm{pC}}$. The linear range reaches up to 190 pC. This covers the signal of 185 pC from fully saturated SiPM with a gain of 10^6.

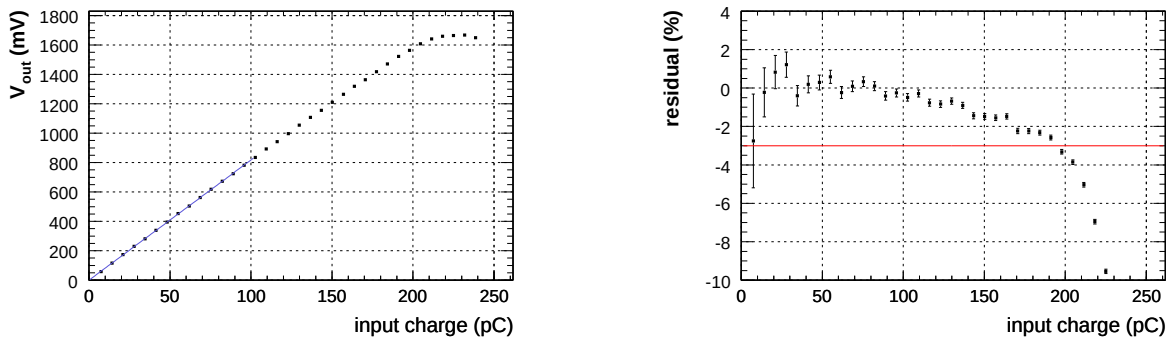

(a) ASIC response function

(b) Residual of the response function to linear fit

Figure 3.3: Physics mode linearity

Rectangular Signals – Time Response

The signals used to research the gain and linearity so far were short pulses optimized to reproduce the rise-time of the SiPM. However, the signal of the SiPM consists not only of a fast part, it has also a long exponential tail which carries roughly half of the charge.

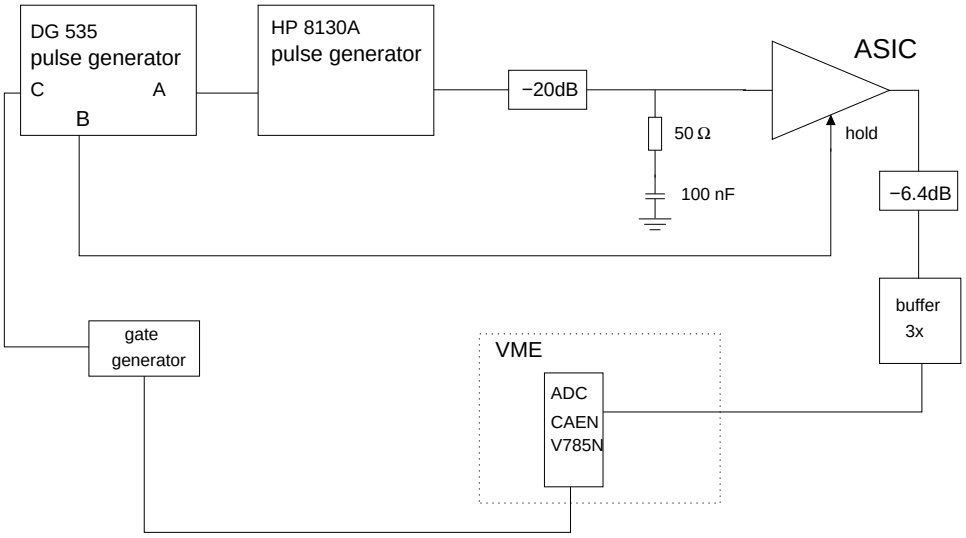

Figure 3.4: Setup to measure the linearity of the ASIC pulses of different width

To see how the gain of the ASIC is related to the length of the input signal a linearity measurement was done for signals of varied length.

For this measurement a rectangular signal with constant amplitude and variable width was used. The used digital pulse generator HP 8130A is able to provide such signals with a rise and fall time of 800 ps. The accuracy of the signal after the -20 dB attenuator was checked with an oscilloscope. The set width was reproduced within 0.1 + 0.3% ns for all used pulse durations. The product of amplitude and width, which is proportional to the injected charge, was found to be accurate within 3%.

The readout of the ASIC signal was done with a VME based system. The used 12bit ADC from CAEN digitalizes the range from 0 to 4 V. The nonlinearity is 0.1% [15].

The charge flowing over the 50 Ω termination resistor can be calculated by $Q = I \cdot t = \frac{V}{R} \cdot t$. Therefore, the input charge is directly proportional to the width of the input signal, as long as the amplitude stays the same. For each input width at least 5 points with a different hold were measured. The amplitude and the position of the output signal maximum were determined by a Gaussian fit of these points.

In figure 3.5(a) the maximum ASIC output amplitude is plotted versus the input signal width. As the signals were not pedestal subtracted the first part is fitted with $y = a \cdot x + b$. Figure 3.3(b) shows the residual

$$y_{res} = \left(\frac{y}{a \cdot x + b} - 1 \right) \cdot 100\% \tag{3.8}$$

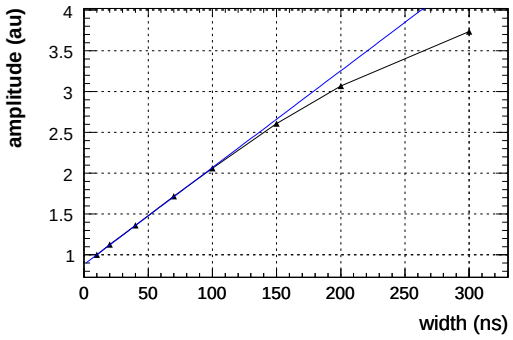

(a) ASIC response function

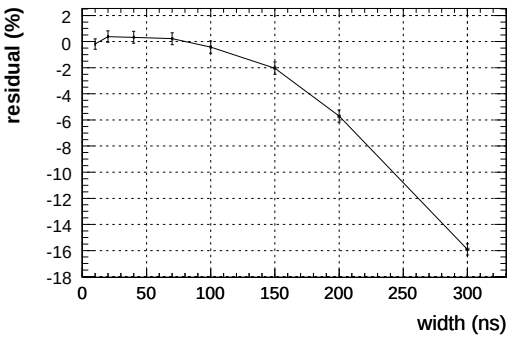

(b) Residual of the response function to linear fit

Figure 3.5: Physics mode linearity

of the signal to this fit. The error for the residual is given by

$$\delta_{y_{res}} = \frac{y}{a \cdot x + b} \cdot \sqrt{\left(\frac{\delta y}{y}\right)^2 + \left(\frac{1}{a \cdot x + b}\right)^2 \cdot (a^2 \cdot \delta_x^2 + x^2 \cdot \delta_a^2 + \delta_b^2)} \cdot 100\% \tag{3.9}$$

The residual plot shows, that the amplification in physics mode is nearly independent of the signal width up to 100 ns. After this point the ASIC amplification decreases.

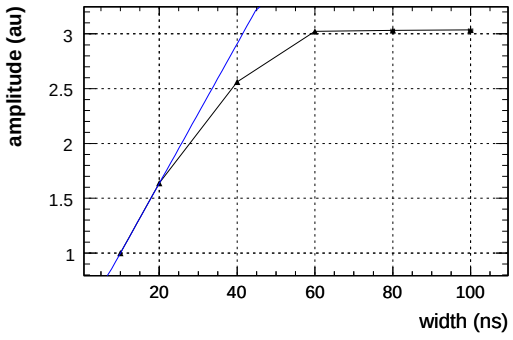

(a) ASIC response function

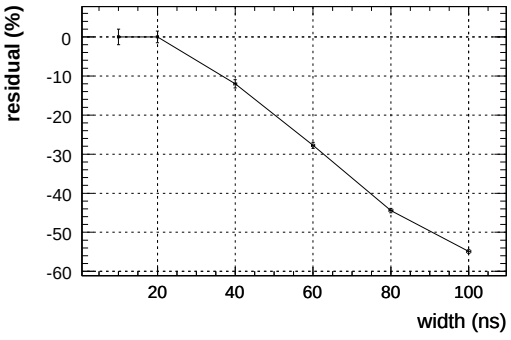

(b) Residual of the response function to linear fit

Figure 3.6: Calibration mode linearity

The same measurement was performed for the calibration mode. Here the output signal does not change anymore for signals longer than 60 ns. For comparison to the physics

mode measurement, the first two points were fitted and figure 3.6(b) shows the resulting residual. But the nonlinear behavior seems to start even before the lowest measured point. Therefore, one has to be careful interpreting this graph. According to the method definition the residuals for the first two points have to lay on zero and the conclusion that the gain is stable in this region may not be drawn. This becomes especially clear when the gain between following points is measured

$$G_i = \frac{V_{out,i+1} - V_{out,i}}{q_{in,i+1} - q_{in,i}} \propto \frac{y_{i+1} - y_i}{w_{i+1} - w_i}, \tag{3.10}$$

where V_{out} is the measured signal amplitude, q_i the input charge, y_i the ADC amplitude and w_i the width of the signal. In figure 3.7 these are plotted versus the average of the width $x_i = (w_{i+1} + w_i)/2$. The gain decreases linearly with the width until it reaches zero. One can assume that the gain increases even more for lower width, which indicates that there is no width range for which the ASIC gain is stable in calibration mode. This method does not allow to measure points of lower signal width with reasonable accuracy.

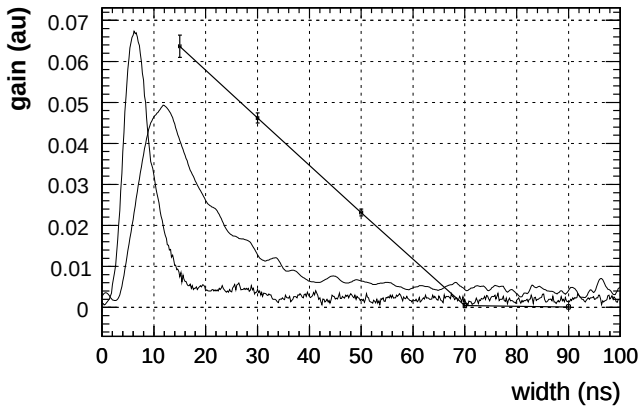

Figure 3.7: Gain development with input signal width in calibration mode, for comparison two SiPM signals of medium (see figure 2.5(b)) and low amplitude (see figure 2.5(a)) are shown. The low signal is enlarged by a factor of 120.

As already explained in chapter 2.2.2 the SiPM signal width varies with amplitude. Such SiPM signals for two different amplitudes are shown under this measurement in figure 3.7. The signals were scaled in amplitude to fit in the graph. The lower SiPM signal amplitude is scaled with a factor of 120 compared to the higher one.

The errors for this measurement are given by

$$\delta_{x_i} = \frac{1}{2} \cdot \sqrt{\delta^2_{w_{i+1}} + \delta^2_{w_i}} \tag{3.11}$$

$$\delta_{G_i} = G_i \sqrt{\frac{\delta^2_{y_{i+1}} + \delta^2_{y_i}}{(y_{i+1} - y_i)^2} + \frac{\delta^2_{w_{i+1}} + \delta^2_{w_i}}{(w_{i+1} - w_i)^2}} \tag{3.12}$$

An increasing input signal width does not only change the output amplitude but also the time of the output signal maximum. This effect may be important as the hold is fixed to a certain time after trigger. The time of the signal maximum was determined as the mean of the fit through the measurements with different hold setting. The results are plot in figure 3.8(a) for calibration mode and in figure 3.8(b) for physics mode.

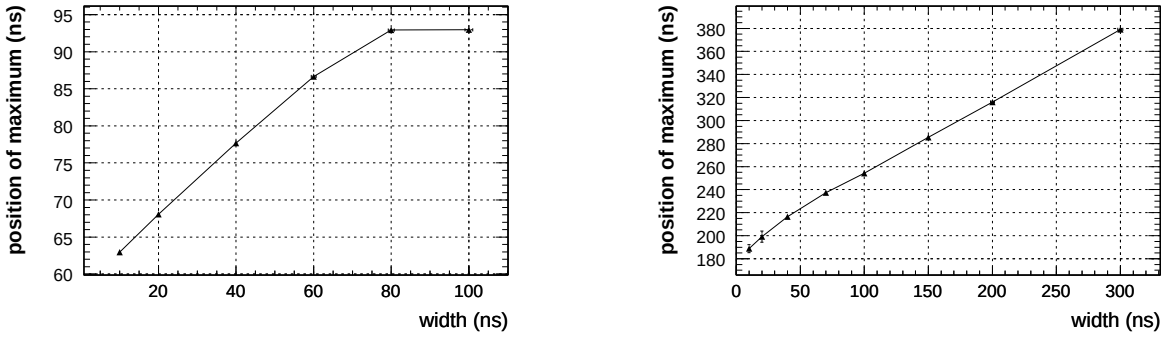

(a) Calibration mode

(b) Physics mode

Figure 3.8: Position of the output signal maximum versus input signal width

The output maximum is reached later for larger signal width in both modes. A linear fit to the lower three points of the calibration mode gives a delay of the maximum for (0.489 ± 0.003) ns per 1 ns change in the input signal width. For higher values the signal position becomes constant. This corresponds to the part of the measurement where the ASIC gain goes to zero. For the physics mode such a measurement gives a relation of (0.9 ± 0.1) ns per ns width increase. In the explored range no saturation was found.

The consequences of this effect should be negligible in the physics mode, as the signal maximum is flat compared to the expected changes. At the upper end of the calibration mode this effect may play a role.

3.1.2 Noise

The noise of the ASIC chip was measured in the same setup as shown in figure 3.1 by removing the input line. To increase the resolution the buffer gain was increased to a factor three. The noise of the setup alone was measured by replacing the ASIC with a 1.2 V battery, and it results in $\sigma_{setup} = (1.64 \pm 0.01)$ channels. Under the assumption that the signal distributions of the ASIC and the setup are Gaussian and uncorrelated, the total noise σ_{tot} is given by

$$\sigma_{tot} = \sqrt{\sigma_{ASIC}^2 + \sigma_{setup}^2} \quad \Rightarrow \sigma_{ASIC} = \sqrt{\sigma_{tot}^2 - \sigma_{setup}^2} \tag{3.13}$$

from which the ASIC noise σ_{ASIC} can be derived. Error propagation leads to following error estimation

$$\delta_{\sigma_{ASIC}} = \frac{1}{\sigma_{ASIC}} \cdot \sqrt{\sigma_{tot}^2 \cdot \delta_{\sigma_{tot}}^2 + \sigma_{setup}^2 \cdot \delta_{\sigma_{setup}}^2} \tag{3.14}$$

The measured mean value of the noise is $\sigma_{tot} = (5.2 \pm 0.1)$ channels with a standard deviation of (0.30 ± 0.08) channels for a sample of 8 chips in calibration mode. This corresponds to an ASIC output noise of (4.94 ± 0.02) channels or (1.72 ± 0.04) mV.

The same measurement was also performed with the longest shaping and gain settings between 0.5 pF and 0.9 pF, which correspond to an amplification range between 8.2 mV/pC to 4.7 mV/pC. The output noise did not show a dependence on the amplifier gain. Following the calculations above, this results in (4.3 ± 0.2) channel, which is almost the same noise as in the calibration mode. Expressed in output voltage this is (1.52 ± 0.05) mV. A more appropriate measure than the output noise is the equivalent noise charge (ENC), which describes the amount of charge which would give the same signal as the noise. As the output noise is independent of the ASIC operation mode, the ENC is determined by the gain. The value calculated for the physics mode is (186 ± 6) fC. For the calibration mode it is (18.6 ± 0.4) fC.

This noise can be compared to the signal from an ideal SiPM with 15 pixel/MIP and a gain of 10^6. The minimum signal to resolve is one pixel in calibration mode, which corresponds to 160 fC. This corresponds a signal to noise ratio of 8.6. The typical signal for the physics mode is one MIP corresponding to 2.4 pC, which leads to a signal to noise ratio of 12.9.

3.1.3 Digital to Analog Converter (DAC)

The gain of the SiPM varies strongly with the bias voltage, as described in chapter 2.2. Consequently the stability and reproducibility of the ASIC DAC are important parameters. To allow an automatic measurement of the DAC response function an electronic setup was built, that adapts the DAC output to the input of the DAQ. Figure 3.9 shows the schematics of this setup. The output voltage of the DAC is sent to a factor 1 amplifier serving as line driver for the 120 Ω input resistor of the DAQ. A 200 Ω resistor serves, together with the 120 Ω resistor as voltage divider. This adapts the 5 V output range to the 2.5 V input range of the DAQ. Over a 10 MΩ resistor a voltage of 15 V is applied to the DAC output. This is done to supply a current to the DAC in the same range, 1 μA to 1.5 μA, like a SiPM would draw.

This setup was calibrated with a DIGISTANT 4462 voltage source in steps of 50 mV. The accuracy of the voltage source is 0.11 mV or better [16]. The relation $y = a \cdot x + b$ between measured ADC channels and set voltage was determined from figure 3.10(a). $a = (0.231888 \pm 0.000002) \frac{\text{mV}}{\text{channel}}$ and $b = (-382.90 \pm 0.02)$ mV. The setup shows a very small nonlinearity up to $V_{in} = 4.60$ V. The amplification stage saturates within 100 mV at this point. Accordingly, the usable range is between 0 V and 4.6 V.

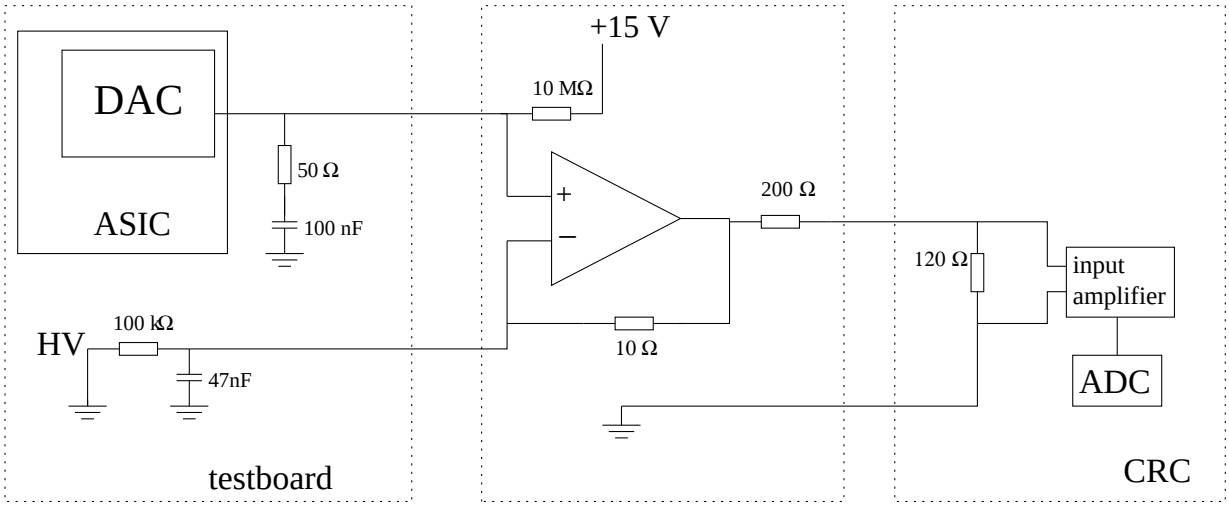

Figure 3.9: Setup to measure the response of the ASIC DAC

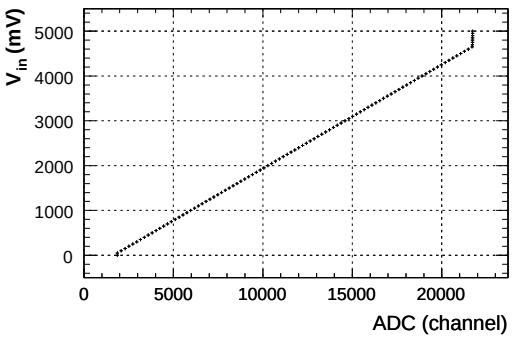

(a) Calibration voltage versus ADC channels

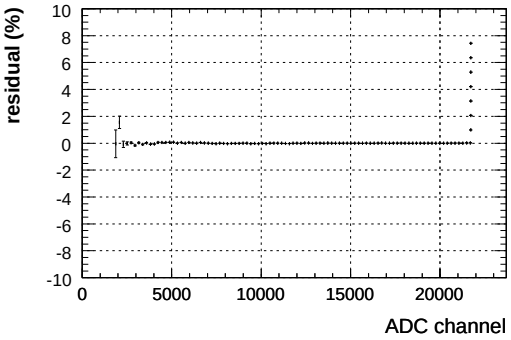

(b) Residual of 3.10(a)

Figure 3.10: Calibration of DAC scan setup

The supply voltage of the DAC is stabilized on the very frontend electronics. The stabilizing components need a minimum difference between supply voltage and the nominal output voltage to work properly. Otherwise fluctuations in the input voltage are not fully compensated. The minimum voltage, for which the DAC supply voltage becomes independent of the frontend electronics supply voltage was measured and is 6.3 V. In the final setup the voltage supplied to the electronics is 6.5 V, taking into account the voltage drop over the supply lines. Hence, the following measurements were done with a supply voltage of 6.5 V.

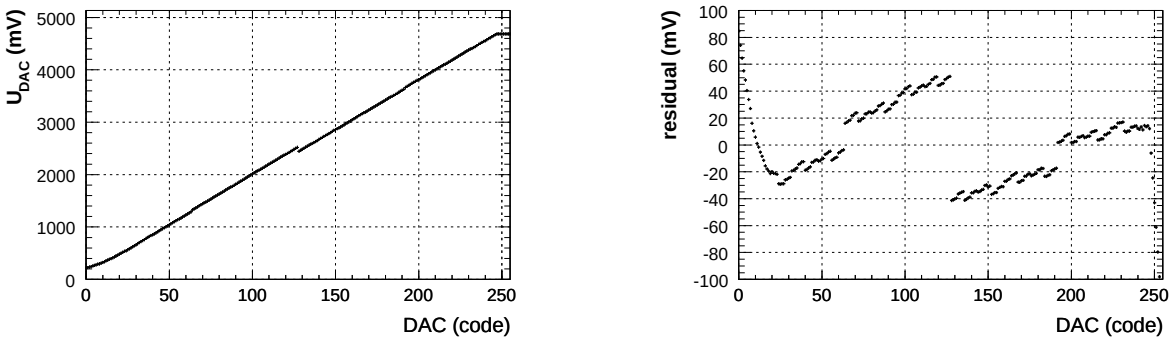

(a) DAC response

(b) DAC response residual

Figure 3.11: DAC linearity

Figure 3.11(a) shows the DAC voltage versus the programmed value as integer as set by the DAQ ranging from 0 - 255 (8bit). The voltage goes to (219.1 ± 0.3) mV instead of zero for a programmed value of zero. This deforms the lowest part of the curve. It becomes linear for values above 16. The measurement shows a saturation at very high values. But this nonlinearity is not an effect of the DAC, it is the limited range of the setup. A linear fit $y = a \cdot x + b$ of the range between 16 and 240 gives $a = (18.377 \pm 0.001)\frac{\text{mV}}{\text{LSB}}$ and $b = (134.4 \pm 0.1)$ mV. The residual of this measurement shows deviations up to 50 mV from the calculated value.

The noise of the DAC was measured with the same setup. The calculation is analogous to the noise measurement shown in section 3.1.2. The noise of the setup was interpolated

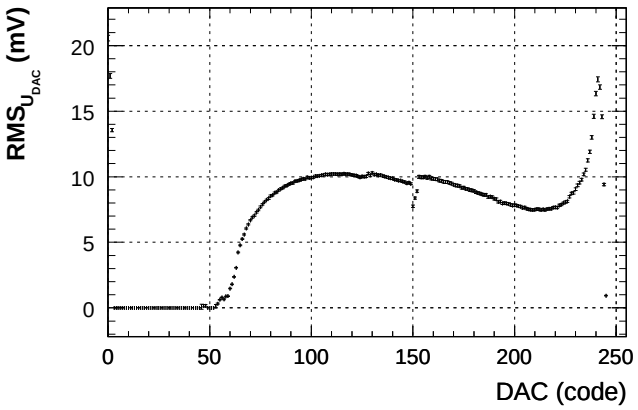

Figure 3.12: Noise of the DAC

from the calibration measurement. Figure 3.12 shows the results. For low DAC values the noise is clearly dominated by the setup. For values above 50 the DAC noise increases up to 10 mV for which it stays up to DAC values around 240. At the end of the DAC range, for values above 240, the noise starts to increase steeply, till the limitation of the measurement setup is reached. The results are summarized in table 3.1.

DAC linear range		16 - 246
maximum error	≤ 50 mV	4 - 246
noise	≤ 10 mV	3 - 232

Table 3.1: Results from the DAC measurement

Accepting an absolute error up to 50 mV, the usable range for the measured DAC is from 4 to 246. The noise of 10 mV introduces a smearing of the SiPM signal of $\approx 0.7\%$, which is an acceptable value. Only relative optimizations of the DAC voltage have to be performed with a certain care, as the signal shows local jumps.

Until now, only one measurement of the DAC was performed at DESY. The result is consistent with measurements done at LAL. For a further analysis of the pattern of the error and to research the channel to channel and chip to chip variations, the setup was extended to six channels for future measurements.

3.2 Data Acquisition System (DAQ)

The data acquisition performs not only the last part of the signal processing, the digitization of the analog signal, it also steers the frontend electronics and does the trigger calculation. Whereas the signal processing in the ASIC chip is analog, the signals processing on the CALICE Readout Card (CRC) is fully digital. The clock on the DAQ card is 160 MHz which gives a 6.25 ns step resolution for all signals sent from the DAQ. Besides the DNL and the noise of the ADC, the influence of this digital steering of the hold signal was examined.

3.2.1 Differential Non Linearity (DNL)

An Analog to Digital Converter translates an analogous signal, i.e. a voltage, to a digital value representing the size of the signal. Whereas an analog signal has a continuous spectrum of values, a digital signal assumes discrete values. Each output value of an ADC corresponds to a certain input range. For a perfect ADC the total input range would be divided into input ranges of the same width, corresponding to the resolution. The transfer function between input and output would be a multi step function with equal step width. In this case the maximum error would be half the width of one step.

In practice an ADC with perfect equidistant steps is hardly realizable. For example the ADC ADS8361 used on the CRC is a Successive Approximation Register (SAR) A/D

converter from Texas Instruments. In an SAR-type ADC the external signal is compared to a variable internal voltage source. The accuracy of the voltage source defines the quality of the conversion process. The differential nonlinearity, which is defined as the maximum and minimum difference between the real step width and the perfect step width of any output step, is one benchmark of such a conversion process.

To measure the DNL a sawtooth signal from a Philips PM5131 function generator was sent to the ADC of the CRC. As the function generator was not synchronized to the DAQ readout, the signals, which are present at the input in the moment of acquisition, are equally distributed over the amplitude range of the signal generator. For a perfect ADC each possible output value of the measured range would occur equally often, within the statistical deviations. Deviations from a homogeneous distribution are a direct measurement of the differential nonlinearity.

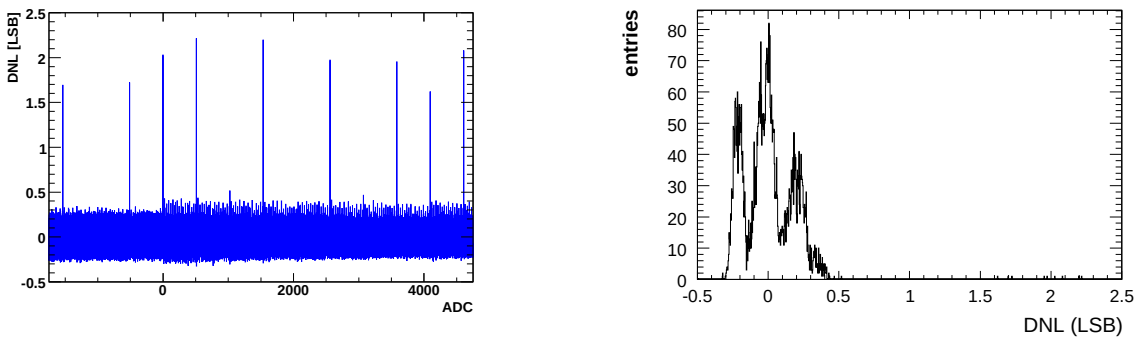

(a) DNL

(b) DNL distribution

Figure 3.13: Differential non linearity of the CRC ADC

Figure 3.13(a) shows this deviations $\frac{N_i - <N_i>}{<N_i>} - 1$ for each bin i. Due to the normalization the height of the bin signal is equal to the width of the corresponding step in the transfer function, measured in the width of the least significant bit (LSB). An average of ≈ 4600 entries per bin were collected, which determines the statistical error on the measurement of one bin to 1.5%. The measured DNL of $^{+2.2}_{-0.3}$ LSB is in accordance with the values from the data sheet of the producer [17]. From the distribution of the signal, shown in figure 3.13(b), it can be seen that for most of the bins the DNL lies between -0.3 and 0.4 LSB. Nevertheless the high peaks show a few entries between 1.5 and 2.5 LSB.

The result is conspicuous by two facts. First, every 512 channels there is a high probability for a step with roughly twice the width of the average bin. The second is, that the distribution of the DNL is not symmetric.

One standard way to reduce the influence of this nonlinearity is to reduce the resolution by joining each n bins to one single bin, before the measured signal is analyzed. For

that reason the influence of re-binning on the DNL was examined. Generally, re-binning increases the value of the LSB by the factor of re-binning. For a better comparability of the absolute bin error all results are shown in respect to the LSB of the full 16 bit resolution.

An improvement in the DNL could only be found for a re-binning with multiples of 4. In figure 3.14(a) - figure 3.14(c) and the corresponding DNL distributions figure 3.14(d) - figure 3.14(f) the effect of re-binning becomes obvious. The distribution of the DNL develops from the multiple peak structure it has without re-binning to a more Gaussian like distribution of smaller width. This reduces the error the DNL introduces for each bin between the high peaks. But the high peaks, which occur roughly every 512 bins, do not average out like the fluctuations in the rest of the range. The relative bin error is only reduced by the factor of re-binning.

One LSB corresponds to 76 μV and in consequence the absolute error on the measurements of signals in the order of 10 mV is negligible. But the high peaks in the spectrum may lead to problems in the numerical data analysis (see section 4.5.2). Based on this a general statement is hard to give, probably the influence of the DNL has to be considered separately for each kind of measurement.

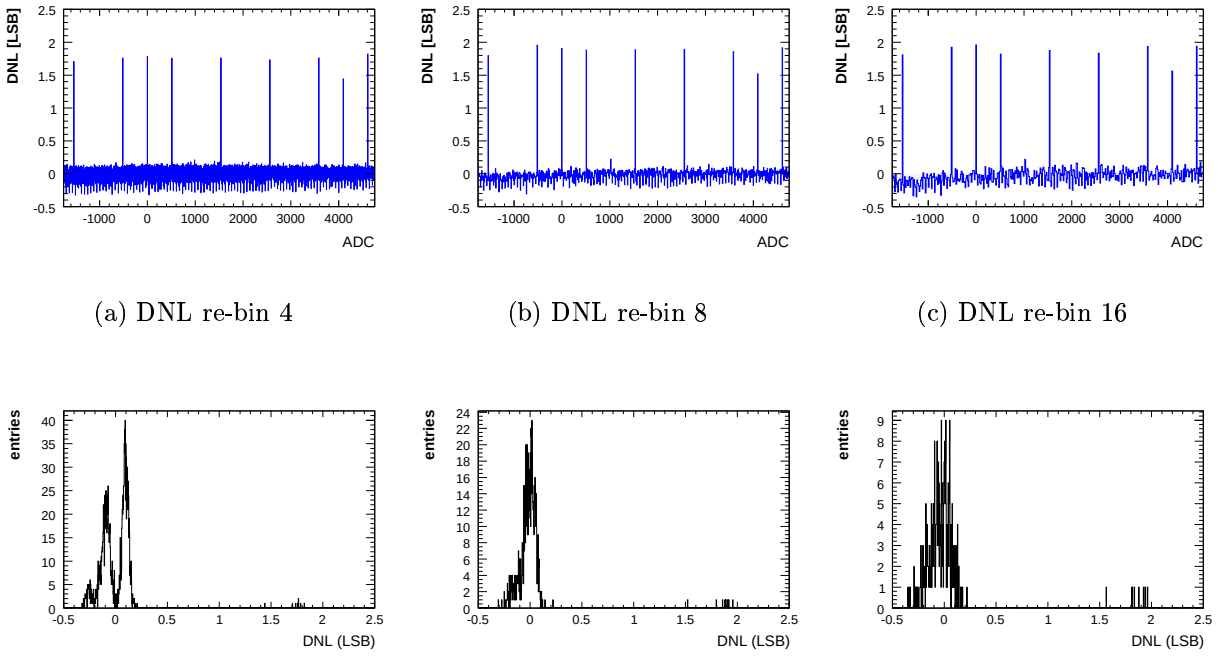

(a) DNL re-bin 4 (b) DNL re-bin 8 (c) DNL re-bin 16

(d) DNL distribution re-bin 4 (e) DNL distribution re-bin 8 (f) DNL distribution re-bin 16

Figure 3.14: Influence of re-binning on the DNL of the CRC ADC. The unit LSB is for comparability always the LSB of the full 16bit ADC range.

3.2.2 Finite Step Width of the Hold Signal

For the calibration of the system, the DAQ initiates a LED pulse from the calibration and monitoring board. The trigger signal sent from the DAQ is called TCalib. The delay between this TCalib signal and the hold signal for the ASIC can be adjusted in steps of 6.25 ns, which corresponds to one clock cycle of the DAQ (160 MHz). The curvature of the ASIC output signal is strong in calibration mode. Therefore, a setup was built to quantify the error that results from an improper timing of the hold compared to the real signal maximum. In the setup shown in figure 3.15, a pulse generator injects charge over a capacitor to the ASIC. The pulse is initiated by the DAQ card, which triggers the pulse generator. The internal delay of the pulse generator is varied by steps of 1 ns.

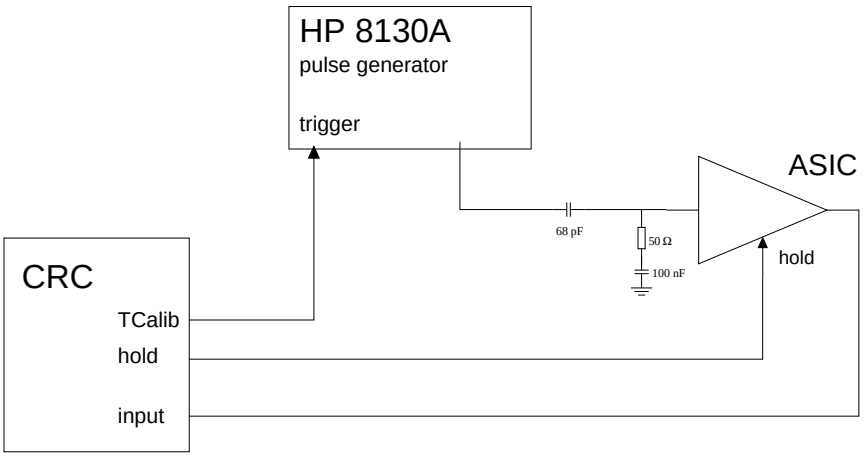

Figure 3.15: Setup to measure the influence of a finite hold resolution

For each delay value of the pulse generator the hold value that gives the highest output amplitude was determined. Figure 3.16(a) shows how the best approximation of the signal maximum moves stepwise with the delay. The resulting maximum amplitude is plotted in figure 3.16(b). The difference between the worst and the best setting is 1.5% of the signal. This introduces a systematical error, if the hold setting is only optimized for the maximum output value without measuring a new gain factor between the physics and calibration mode after a change in the hold value.

The error described above is more of theoretical nature, as an individual measurement of the gain between the two modes for each channel is mandatory for several reasons.

3.3 Combined System

3.3.1 Adaption of ASIC and DAQ

Following from the measurements in section 3.1.1, the linear output range of the ASIC in calibration mode ends at 1.3 V. The gain of the physics mode was chosen in such a way

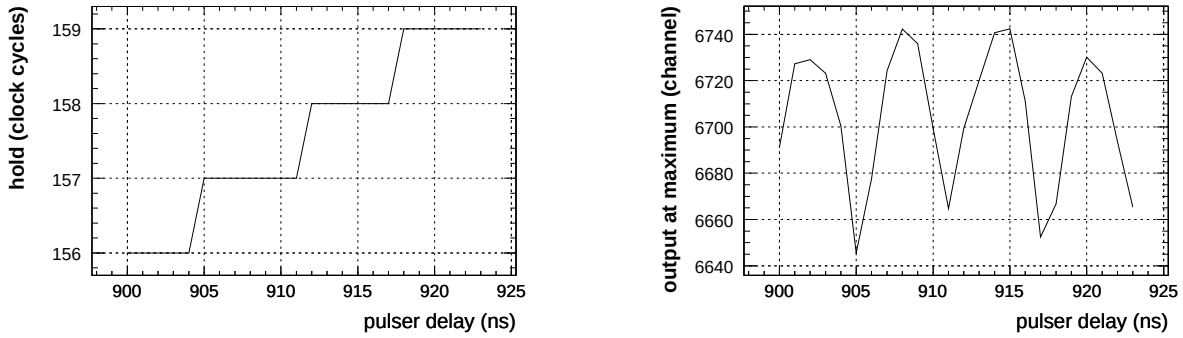

(a) Best hold setting

(b) Maximum amplitude

Figure 3.16: Influence of the finite hold resolution

that a fully saturated SiPM signal lies within the linear range of the ASIC which results in an almost similar linear output range. The input range of the DAQ lies between -2.5 V and +2.5 V. To avoid pedestal fluctuations the reference of ASIC output and DAQ input are both set to 0 V. This leaves the range between 0 V and 2.5 V as possible input range of the DAQ. The line driver gain of the very frontend electronics was set to a factor of 2.0 to extend the ASIC output range to the input range of the DAQ. This cuts a little of the linear range of the ASIC but gives a better resolution of the real SiPM from the mass production. The first samples show a smaller gain of only $\approx 0.5 \cdot 10^6$, so the slightly reduced ASIC output range of 1.25 V covers these SiPM easily.

3.3.2 Noise

The noise for the final readout chain was measured with the DAQ itself. The results are summarized in table 3.2.

setup	σ (channel)	σ $(\mathrm{mV})^2$
DAQ	1.39 ± 0.06	0.053 ± 0.002
DAQ + mother board (MB)	1.39 ± 0.06	0.053 ± 0.002
DAQ + MB + frontend electronics in calibration mode	45 ± 2	1.71 ± 0.08
DAQ + MB + frontend electronics in physics mode	36 ± 2	1.37 ± 0.08

Table 3.2: Results of the noise measurements with the DAQ

Comparing these values to the measurement in section 3.1.2 shows, that the noise of the full system is the same as for the ASIC alone. The noise is fully dominated by the ASIC noise.

3.4 Conclusions from the Electronic System Measurements

Several aspects of the ASIC chip were tested. The gain and noise performance are good enough that relaxed criterions for the SiPM can be applied, which is necessary as gain and light yield do only approximately fulfill the design parameters. The linearity for signals of fixed width give a deviation of less than 3% in the relevant range.

The variation of the ASIC gain with the signal shape in calibration mode is expected to be negligible in the range of the gain measurement. SiPM saturation does not play a role at such low amplitudes and the shape of the signal is stable. An observed dependence of the ratio between the physics and calibration mode on the used SiPM series is explained by this effect. An individual measurement of the gain ratio is thus necessary for all channels. The exact influence on the inter-calibration between the two ASIC operation modes has to be quantified in further studies.

The absolute accuracy of the ASIC DAC, including DNL and nonlinearity, was determined and is ± 50 mV over 95% of the total range. This is good enough for our requirements. Only if the SiPM signal should be adjusted by a relative voltage change the big jump of 100 mV in the middle of the range should be avoided. The noise in the bias voltage is acceptable with a maximum of 10 mV over 90% of the range.

The measurements of the mother board and the DAQ showed no influence on the noise performance of the readout electronics, which is the optimal result. As an individual measurement of the gain ratio between the ASIC modes is already necessary as described above, the influence of the limited hold accuracy does not matter.

The influence of the differential non linearity in the ADCs of the DAQ is not fully predictable. The SiPM gain measurements described in section 4 do not show a dependence in the result, but the interpretation of the data gets more complicated. How other measurements will be influenced has to be studied.

Chapter 4

Integration of SiPM and the Dedicated Very Front End Electronics

The studies of SiPM presented sofar, were done in small laboratory setups. In these setups the SiPM signal was measured directly with charge sensitive ADCs. The physics prototype detectors AHCAL and TCMT form a more complex system. One difference is the use of the dedicated electronics which is not a pure charge sensitive one. Another peculiarity are the practical limitations in individually optimizing every channel of a 8000 channel system.

The gain is an important parameter for the description of the saturation behavior of a SiPM, and as consequence a necessity for the calibration of the detectors. The aims of the research reported in this chapter are to transfer the laboratory measurement to the integrated system. Therefore, next to the development of an accurate description of the signal, an understanding of the requirements on production uniformity is necessary.

The statistics which is needed for a calibration determines the time which has to be invested. When the system should be calibrated during data taking at a test-beam this directly competes with the amount of "physics" data which can be collected during a test-beam period. So the minimum number of events necessary to obtain a reliable calibration is an important quantity.

In addition, effort should be made to supply a system that can be calibrated with a minimum (possibly one) of required configurations. If the variance in the light distribution system becomes too large, it is not possible to calibrate all channels with one light intensity setting. This would increase the time for the calibration, as the measurement has to be done repeatedly.

In the AHCAL, each 18 scintillator tiles are illuminated by a single LED, where the light is transferred over a bundle of optical fibers. The light distribution system was optimized in such a way, that the ratio between brightest and dimmest fiber is smaller than 2. This is done to ensure that all SiPMs, illuminated by one LED, receive light signals in the range appropriate for the gain measurement at the same time.

4.1 SIPM Signal and Gain

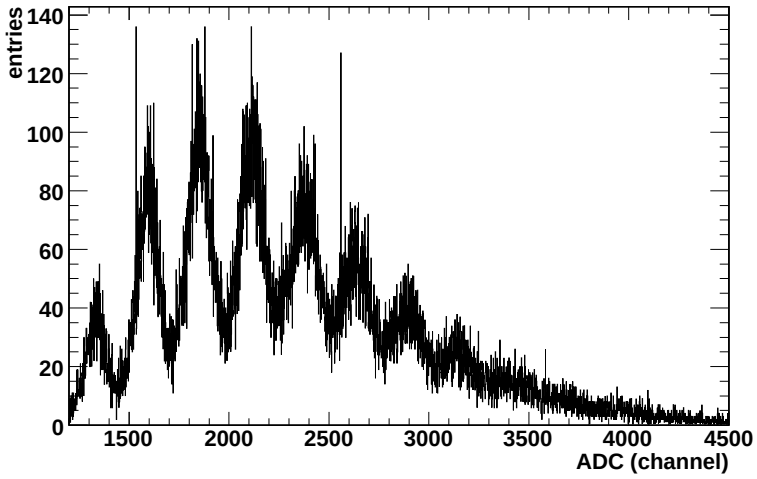

Figure 4.1: Typical spectrum of a SiPM

Figure 4.1 shows a SiPM spectrum measured with the prototype electronics. As described in section 2.2.1, a SiPM gives a signal

$$A = N \cdot Q_{pix} \qquad N = 0, 1, ..., 1156 \tag{4.1}$$

which is N times the charge Q_{pix} of a single firing pixel. The gain of a SiPM $G = \frac{Q_{pix}}{e}$ is defined as the ratio between the charge released from one firing pixel and the electron charge e. The charge created in pixel will vary from avalanche to avalanche due to fluctuations in the multiplication process σ_{pix}. Additionally small differences between the pixels will distribute the gain for the different pixels around some mean value with σ_G. Assuming, that all these distributions are Gaussian and uncorrelated, the distribution of the output signal A is

$$\sigma_A = \sqrt{\sigma_{elec}^2 + N \cdot \sigma_{pix}^2 + N \cdot \sigma_G^2} \tag{4.2}$$

Measurements done by the producer show, that σ_{pix} and σ_G are small compared to the noise σ_{elec} of the prototype electronics and can normally be neglected for signals of a few pixels. However, σ_{pix} and σ_G limit the separation of single pixel peaks for large N.

The output signal value is proportional to the input signal charge for the used electronics. Consequently the distance between the mean signal $\Delta_i =< A_{i+1} > - < A_i >$ for $i+1$ and i fired pixels is proportional to the charge of one pixel.

Idealizing the signal from the SiPM so that Δ_i is independent of i and the signal width $\sigma_A = \sigma_{elec}$, the distribution measured would follow

$$f(x) = \sum_{i}^{1156} P(i,\mu) \cdot g(x - i \cdot \Delta) \tag{4.3}$$

where the occurrence of i photons detected follows a Poisson distribution

$$P(i,\mu) = \frac{\mu^i \cdot e^{-\mu}}{i!}$$

around the mean μ. The second function is the Gaussian distribution of the measurement electronics

$$g(x) = \frac{1}{2\pi \cdot \sigma_{elec}} \cdot e^{-\frac{\left(x - x_{ped}\right)^2}{2 \cdot \sigma_{elec}^2}}.$$

For a real SiPM the assumption of a Poisson distribution for the number of fired pixels does not hold. The presence of optical crosstalk introduces a probability of $\approx 30\%$ that photons generated in the Geiger discharge of one pixel fire a second pixel, destroying the assumption that each pixel is fired independently. As this does not effect the mean peak position, the gain can be measured without an exact knowledge of this distribution. Therefore, the frequency of a distinct number of firing pixels is a free parameter of the fit.

4.2 Determination of the Fit Function

For the calibration of the full AHCAL detector, the gain has to be determined for ≈ 8000 channels. This introduces more requirements than only accuracy for the fit. The fit routine has to run as much as possible independently from human interaction. A further constraint is the processing power and memory usage of the gain calculation.

Two types of distributions were tested for practicability. A distribution of equally spaced Gaussians (equation 4.4) and the sum of Gaussians in equation 4.5, which leaves all parameters free.

$$f(x) = A_i \cdot \frac{1}{2\pi \cdot \sigma_i} \cdot e^{-\frac{\left(x - i \cdot \Delta - x_{ped}\right)^2}{2 \cdot \sigma_i^2}} \tag{4.4}$$

$$f(x) = A_i \cdot \frac{1}{2\pi \cdot \sigma_i} \cdot e^{-\frac{(x - x_i)^2}{2 \cdot \sigma_i^2}} \tag{4.5}$$

As already mentioned, the electronic noise dominates the width of the single peaks. Accordingly, both distributions were tested with $\sigma_i = \sigma_{elec}$, too.

4.3 Determination of the Starting Values – Peak Finder

One problem, that has to be solved, is the determination of the starting values for the fit, if it should run automatically. The pedestal position and width can easily be determined with a dedicated pedestal run. A first approximation of the position of the single peaks in the histogram is more complicated. The ROOT environment (see [18]), which was used for the analysis, offers in general a peak finder class which derives the peak positions from a Fourier analysis of the histogram. But the reliability of this peak determination does not fulfill the needs of a 8000 channel system.

Therefore, a dedicated peak finder for the spectra of SiPM was developed. This peak-finder distinguishes the minima and maxima of the spectrum by determining where the derivative of the spectrum is zero.

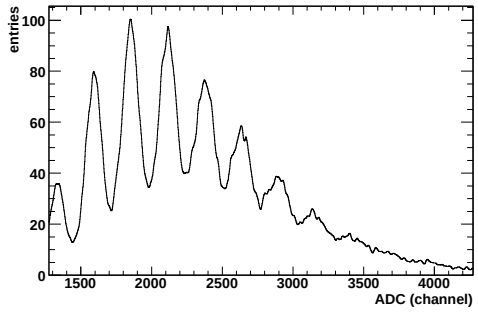

(a) Histogram after smoothing

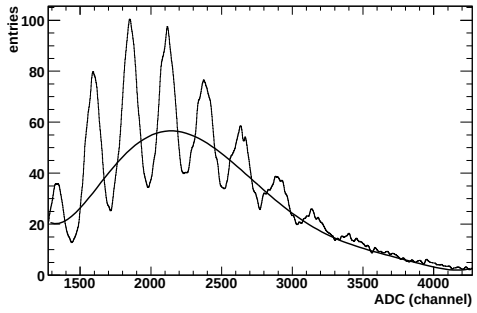

(b) Fitting polynomial

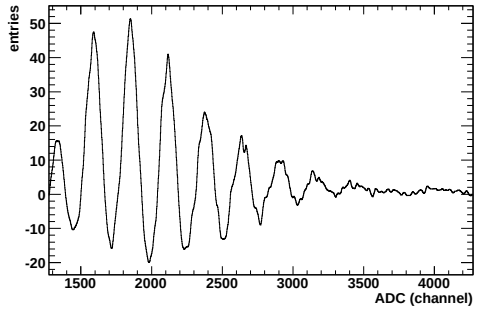

(c) Histogram after the fit function was removed

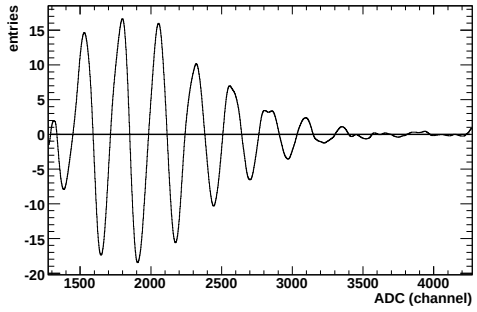

(d) Differentiated histogram

Figure 4.2: Working principle of the peak finder

During the development of this algorithm, it became obvious that the DNL of the ADC fakes the presence of additional peaks. To get rid of this effect, the histogram was smoothed by applying a floating average (figure 4.2(a)).

Another disturbing effect is the "pile up" of the peaks around the mean in large signals. It would shift the derivative to positive values and some extrema may not be found. To reduce this, a sixth order polynomial is fitted to the signals extending a certain range. The obtained function is removed like a "background" signal from the histogram (figure 4.2(b) and figure 4.2(c)).

The modified histogram is now differentiated (figure 4.2(d)). To distinguish the position the derivative is searched for the crossings of the zero line. The found positions of these crossings are divided into maxima and minima.

Knowing both, minima and maxima of the signal offers a very reliable way to check the quality of the found peaks. In a first approximation of the distance, all found peak positions are accepted where distance between subsequent maxima and the distance between subsequent minima does not vary by more than 32 channels. This is a very strict requirement and discards some acceptable peaks. All peaks, that do not vary by more than one eighth of the distance retrieved before, are accepted in a second selection to extend the number of accepted peaks.

Each found peak is fitted with a single Gaussian in the range given by the surrounding minima. This fits are done in the original histogram, as the applied floating average does broaden the width of the peaks. ROOT offers a reliable automatic generation of the fit start values for a single Gaussian. So no further effort is necessary to get reliable results.

Sometimes the peakfinder finds peaks in the tail of the signal, which are hardly to fit. The relatively small statistics of these peaks and the large width due to the high order of these peaks give a very indistinct position of the maximum. To avoid a biasing of the full fit due to these peaks, the peak with the highest order is removed from the set of accepted peaks. This is repeated as long as the RMS of the distances is not smaller than 5% of the average distance calculated from the set of accepted peaks.

The results from these single fits represent the set of starting values for a fit of combined Gaussians. Figure 4.3(b) shows the final multi Gaussian fit.

4.4 Choice of Fit Method

For the study of the different fit methods, a set of gain calibration runs was taken with the second AHCAL module. One LED was driven by a prototype of the calibration electronics and it illuminated 18 tiles, from which only 15 were read out due to problems with the electronics. Five runs were taken with different light amplitudes and at least 10k events.

Whereas the fits with formula 4.5 showed constantly good results, the results obtained using equation 4.4 showed some problems. When the peak width is not fixed the fit does not converge in most of the channels. An optical check of the result, where the width

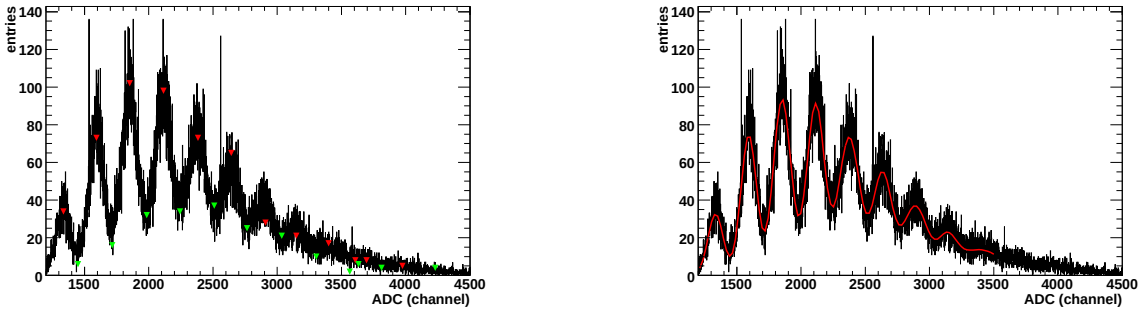

(a) Found minima and maxima

(b) Multi Gaussian fit

Figure 4.3: Output of peakfinder and multi Gaussian fit

was fixed to σ_{elec} shows that the function describes the signal poorly in a fraction of the channels. This makes it necessary to use the fit with variable distance between peaks.

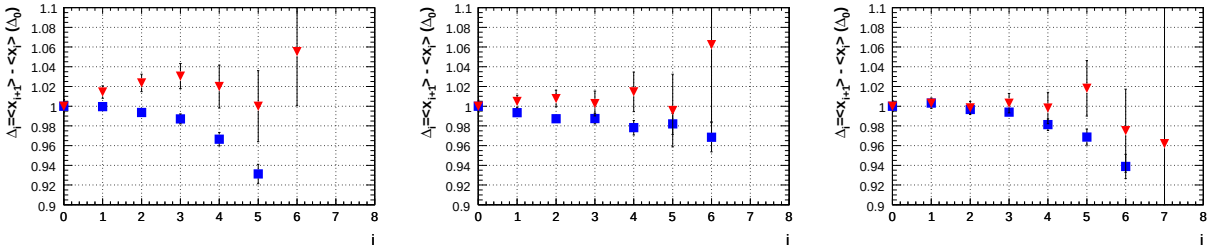

(a) Channel 7

(b) Channel 8

(c) Channel 9

Figure 4.4: Comparison of fits with constant peak width σ_{elec} (rectangles) and variable width (triangles). i denotes the distance between peak $i+1$ and i.

Although the width of the single peaks is dominated by the noise of the electronics, the increase of the width with the order of the peak may not be neglected. Comparing the results from a fit with fixed width to the results obtained using a fit with variable width shows that fixing the width introduces a systematical of the distance between peaks to lower values with increasing order of the peaks. This effect can be seen in figure 4.4 where the calculated distance is plotted against the order i of the peaks from which it was determined. The fit with variable width shows a stable gain within the measurement errors, whereas the fixed width shows a clear trend to lower values, especially regarding

the small estimated errors.

Summarizing the efforts to describe the SiPM spectrum with as few parameters as possible, it has to be admitted, that until now no adequate description exists of the complete SiPM spectrum which provides convincing fit results. Finally the used fit has to be considered as an independent measurement of the peaks with different order. The large number of free parameters does not only increase the processing power needed for the fit but also introduces more fluctuations in the result.

A different approach to measure the gain is the use of a Fourier transformation. The adaption of this algorithm to the needs of our electronics is ongoing, but once applied the results may be superior in two aspects. First, in the frequency domain the distance between the peaks corresponds to one distinct value, that can be determined by a single fit using all available information. The second improvement which can expected is that the DNL of the ADC, which is a major disturbance for the multi Gaussian fit, appears at different frequencies than the gain signal.

4.5 Fit Quality

Until now, the judgment of the quality of the results was done by visual inspection, which is appropriate for the comparisons done so far. A more objective tool is necessary to test how good the real data matches the theoretical description.

In fact, the used fit method, which applies the least squares method, offers such a value, the χ^2.

4.5.1 The χ^2 Test

Each bin of the histogram can be seen as an individual measurement of the distribution $f(x)$. If the distribution of the individual bins is Gaussian, the χ^2 is defined as

$$\chi^2 = \sum_i^N \left(\frac{y_i - f(x_i)}{\sigma_i} \right)^2. \tag{4.6}$$

The χ^2 itself follows the distribution

$$P(\chi^2, \nu) \cdot \mathrm{d}\chi^2 = \frac{\left(\frac{\chi^2}{2}\right)^{\frac{\nu}{2}-1} \cdot e^{-\frac{\chi^2}{2}}}{2 \cdot \Gamma(\frac{\nu}{2})} \cdot \mathrm{d}\chi^2 \tag{4.7}$$

for all $f(x)$. The parameter $\nu = N - n$ is the number of degrees of freedom, in this case the number of bins N minus the number of parameters determined in the fit n. The mean and variance of this distribution are

$$\mu = \nu, \qquad \sigma^2 = 2 \cdot \nu.$$

Comparing the measured value of χ^2 for an assumed distribution $f(x)$ to the expected value offers a test of the hypothesis that the real data follows the distribution $f(x)$. The ratio $\hat{\chi}^2 = \frac{\chi^2}{\nu}$, called the reduced χ^2, should be 1. This expresses the fact, that the average fluctuation between theoretical and measured value is one σ. The maximum expected deviation from $\hat{\chi}^2 = 1$ depends on ν. The measured $\hat{\chi}^2$ is normally larger than the ideal one, as deviations from the distribution $f(x)$ will increase χ. Only if the error on the bins is overestimated χ^2 becomes systematically smaller than expected.

The probability

$$p(\chi^2, \nu) = \int_{\chi^2}^{\infty} P(u, \nu) \cdot \mathrm{d}u \tag{4.8}$$

to find the same or a larger, and thus worse, χ^2 when repeating the measurement with the same number of degrees of freedom gives the quality of agreement between theory and measurement, independent of ν.

4.5.2 Application of the χ^2-Test

The χ^2-test demands as condition that the distribution of the single bins is Gaussian. Regarding the DNL, which introduces an individual systematical error for each bin, this condition is not fulfilled for the spectra measured with our electronics. Before calculating the χ^2, this has to be treated.

The analysis of the DNL (see 3.2.1) shows that the DNL itself does not follow a Gaussian distribution. This prohibits a statistical treatment of the DNL by quadratically adding the width of DNL σ_{DNL} and the expected statistical fluctuation of each bin σ_{Gauss}. After re-binning, the DNL shows a nearly Gaussian distribution if the bins with a DNL around 2 LSB are excluded.

The fit results obtained by three methods were compared, in order to see the influence of the DNL on the fit result and if necessary to find an applicable correction.

1. Fit of the unalternated measurement with $\sigma_i = \sqrt{N}$
2. The DNL measurement shown in section 3.2.1 was used to correct each bin individually.

   $$A_{cor,i} = \frac{A_{meas,i}}{f(i)},$$

   where $f(i) = \frac{A_{DNL,i}}{<A_{DNL}>}$ is the ratio between measured and expected entries in the DNL measurement. The width of the combined distribution of DNL and measurement is the quadratic sum of the single distributions $\sigma_i = \sqrt{N_i + (\sigma_{DNL} \cdot N_i)^2}$.
3. The histogram was re-binned by merging each 8 bins. The error for each bin was recalculated, assuming that the distribution of the DNL is Gaussian. $\sigma_i = \sqrt{N_i + (\sigma_{DNL} \cdot N_i)^2}$, where the RMS of the DNL distribution was used as σ_{DNL}.

Method 2 is the the only one where the bias of the DNL should play no role and the error of the bin can be expected to follow a Gaussian distribution. Therefore, this correction was used to judge the agreement between signal and theory. All fits that converged showed a $\hat{\chi}^2$ between 1.1 and 2.0. Calculating the p from equation 4.8 shows probabilities for such values in the order of 10^{-3} to 10^{-14}. The clear conclusion is that a multi Gaussian fit does not describe the SiPM signal perfectly. But how bad the disagreement is needs some discussion.

In general, the accuracy and sensitivity of the χ^2-test depends on the number of degrees of freedom. The range over which the signal is spread varies between 1500 to 4000 bins. This high number in combination with high overall statistics makes the p-value sensitive to small disagreements.

But there are as well effects which lead to a non Gaussian distribution of the signals. Until now, three main effects are known.

a) The dark noise of the SiPM leads to a baseline fluctuation. This fluctuation is asymmetric due to the shaper used in the ASIC.

b) The fluctuations in the avalanche process have an asymmetric component. The maximum charge that can be created is limited by the geometry. But sometimes the avalanche quenches before it has fully developed. Depending on the quality of the SiPM, pixel signals of only a fraction of the average signal charge occur with low frequency. So the probability for lower signals is bigger than for higher signals.

c) Sometimes imperfections in the production lead to a few pixels in the SiPM with different gain. These will destroy the Gaussian shape of the total signal.

These effects will mainly affect the tails of the single pixel signal distributions. The relevant parameter for the gain measurement is the peak mean position, where these effects should play a minor role. Considering the fact, that the average $\hat{\chi}^2$ is between 1.2 and 1.3 and thus the average disagreement between theory and experiment is in the order of two to three tenth of a standard deviation one can conclude that the accuracy of the gain determination is acceptable for our purposes.

A precise measurement of the DNL for each of the 450 ADC channels is a not negligible effort and would cause delays. Therefore, the results were compared with the uncorrected fit and method 3 was tested as alternative. Already the difference between uncorrected and corrected data is small enough to use an uncorrected measurement to determine the gain without introducing any serious degradation of the result.

Figure 4.5 shows the distribution of the difference between the gain obtained by method 2 and 1. The maximum difference is not bigger than 1%, the RMS of this distribution is smaller than 0.2% and no systematical difference can be observed.

However, the $\hat{\chi}^2$ cannot be used to check the fit quality without correcting the DNL. A check of the fit result is done by comparing the distance between different peaks as alternative. This method requires at least three visible peaks, so that two distance measurements can be done. A fit is considered as corrupt, if the two distances vary for more than 3%.

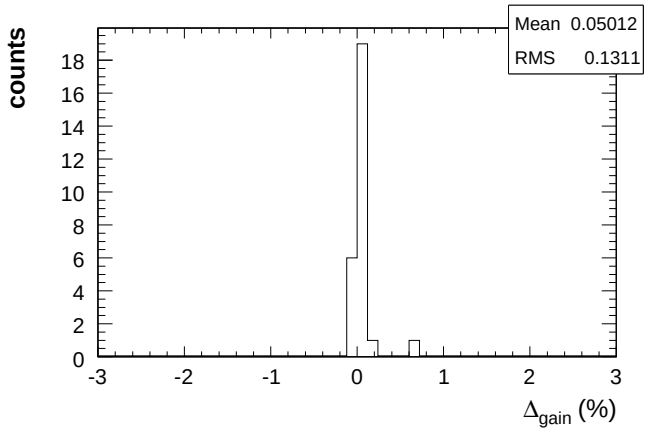

Figure 4.5: Dependence of the measured gain on the DNL correction; $\Delta_{gain} = \frac{G_{Met.\ 2}}{G_{Met.\ 1}} - 1$

Despite the fact that the expected improvement for the last method is not too high, the re-binning had negative effects on the stability of the automatic fit procedure. Thus, this approach was not followed any further.

4.6 Robustness of the Fit

The time needed for a calibration of the system should be as small as possible. Accordingly, one wants to know which number of events is necessary to obtain an accurate result. Additionally, the maximum light spread which can be accepted in the light distribution system is a value of interest. The performance of the fit was tested on the second module produced for the AHCAL. This module, produced in the startup phase of the production process does not yet fulfill the expected quality criterions. The light spread was measured as a factor 3.5 on the tested LED channels and exceeds the required value of a factor of 2 or less. In addition three of the 18 channels had electronic problems, so the test was limited to a sample of 15 SiPM.

A measurement with 5 different light amplitudes was performed. The smallest light intensity was set to such a value, that in all channels at least 3 peaks (including the pedestal peak) of the spectra were found by the peak finder. Starting from this, the light flux was increased between the measurements until it reached a factor of 3.5 for the last measurement.

For each light setting the fit results were checked for different statistics. Table 4.1 shows the results. For the two lowest light settings all fits converged already with a statistic of 12000 events. When the light is increased further, the broadening of the signal distribution reduces the events in a single peak. Consequently the fit for the channel with the most light fails, but it can be recovered by increasing the statistics. As the peak finder starts from the pedestal peak, the pedestal peak has to be visible in the spectrum. This leads

light intensity	converged fits **statistics:** 12k	24k	75k	150k
1	15			
1.4	15			
1.9	14	15		
2.5		13	13	14
3.5		10	12	12

Table 4.1: Number of converged fits depending on the input light and used statistics.

to a limit for the maximum light in a channel that can be fitted. The measurements for further increased light show, that not all channels can be recovered anymore with higher statistics.

Using a measurement of at least 24000 events the fit procedure converged on all channels for a maximum light spread factor of roughly 6.5, taking into account the spread of the module and the variation by increasing the LED intensity. However, this is only a measure of the efficiency of the peak finder. How the quality of the fit is affected by the change in the light and the used statistics has to be investigated separately.

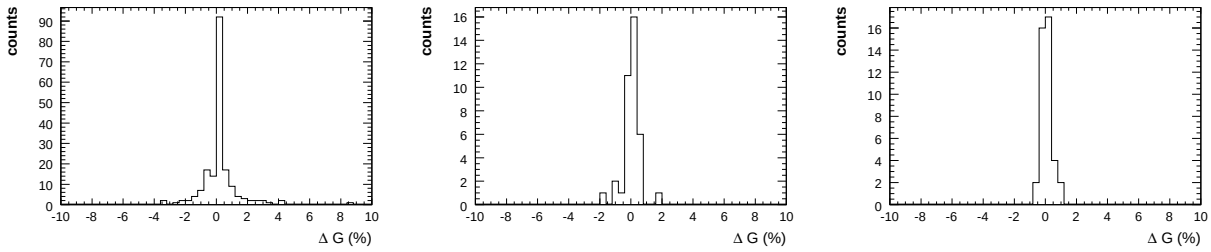

(a) less than 6000 epp (b) 6000 to 10000 epp (c) more than 10000 epp

Figure 4.6: Variation of the gain in dependence of the statistics. The gain was compared to the measurement with the highest statistics. The number of events per peak (epp) was calculated as the average of the 3 highest peaks in the spectrum.

To see what statistic is needed for an accurate measurement, the fits of histograms with reduced statistics were compared with the fit from the measurement with full statistics. Due to the spread in the light distribution, the total statistic is a poor indicator of the statistics used in the relevant part of the fit. To achieve a better comparability of the measurements, the average number of events in the three highest peaks was used as criterion. The results were grouped in three ranges, less than 6000 events per peak, between 6000 an 10000 events per peak and more than 10000 events per peak (epp). The results are shown in figure 4.6.

Whereas the measurements show deviations smaller than 1% for statistics above 10000 epp, the measurements for less than 6000 events show significantly larger fluctuations. Though 77% of the results are within 1% accuracy, 11% show an error of more than 10%. The intermediate range shows a fluctuation of roughly 1%, which seems to be acceptable.

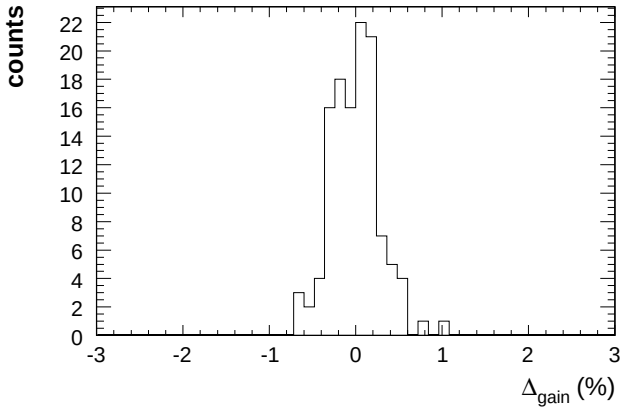

Figure 4.7: Histogram of differences between gain for increased light settings compared to the lowest light setting.

Finally the influence of the light setting itself was tested. The development of the mean with increasing light was analyzed for all channels, using the maximum statistic available. Some fluctuations were observed, but no systematical effect. Figure 4.7 shows the summarized measurement of all channels and all light settings. The fluctuations are smaller than 1%.

These measurements are performed with the highest available statistics, larger than 10000 epp, so that the statistical fluctuations can be neglected. Due to the fact, that the light does not show any systematics, the measurement displays the reproducibility. The fluctuations show the systematic errors in the measurement.

Combining all the measurements, it can be concluded that a measurement of the gain with one setting is for sure possible with a light distribution less than a factor 2. The statistic needed for a measurement with an accuracy of 1% is 6000 events per peak or more in the highest 3 peaks. Depending on the average light setting this corresponds to an estimated total statistics between 30000 and 60000 events in one calibration measurement.

4.7 Application of the Gain Measurement

The gain determination procedure developed sofar was tested on a cosmic ray setup. This setup consisted of three modules in a stack of steel plates. At the time of measurement, the final calibration and monitoring electronics was not available. Therefore, only three

LEDs in one of the module could be used (The positions of the LED, marked as 5,7,8, are kept for reference). Additionally the light spread between the LEDs could not be adjusted, which made it impossible to take the data in one run.

To save time during the calibration procedure and cover the high spread in the light distribution, the calibration data was not taken at a fixed light amplitude. The data from several light settings were joined in one histogram. Due to the large spread in the intensity of the LEDs this did not compensate the variations properly. Figure 4.8 shows how this affected the measured spectra. A large fraction of the channels illuminated by LED 5 had a too low light intensity for a fit. The channels that could be fitted had huge statistics in the relevant peaks. For LED 7, which had a medium light setting, all channels could be fitted, but the relevant statistic did not reach the number for a measurement with 1% accuracy. LED 8 showed the highest light intensity. As a consequence, the statistic is reduced significantly in the part which is fit and the fit failed for some channels.

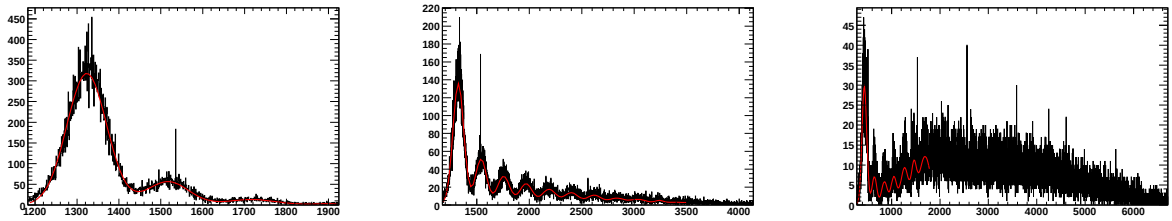

(a) LED 5 (b) LED 7 (c) LED 8

Figure 4.8: Typical spectra for the used LEDs in the cosmics setup.

150 gain measurements were taken over 24 hours. At the same time, the temperature was measured with the built-in sensors in the module. To distinguish the temperature dependence of the SiPM gain the change in gain Δ_{gain} was plotted against the temperature and fitted with a straight line. The computed value for $\frac{\mathrm{d}G}{\mathrm{d}T}$ is $(-1.7 \pm 0.1)\ \frac{\%}{\mathrm{K}}$ for LED 5 and $(-1.70 \pm 0.05)\ \frac{\%}{\mathrm{K}}$ for LED 7. These results confirm the specification of the producer $\frac{\mathrm{d}G}{\mathrm{d}T} = -1.7\ \frac{\%}{\mathrm{K}}$. The results from LED 8 were spread too much to achieve a reliable fit. Figure 4.9 shows the plots for LED 5 and LED 7.

first the temperature increased and went down again later in the 24 hour period. Since the temperature sensor was mounted not directly at the SiPM position in the module, the temperature measured may not be exactly the temperature of the SiPM. This results in a hysteresis of the curve, as can be seen in figure 4.10. To distinguish the gain, a period of falling temperature was used for LED 7 to diminish the bias on the measurement. For LED 5 the statistical fluctuations are dominant compared to the hysteresis effect.

To investigate the accuracy of the gain measurement the data was grouped into samples taken in a time short enough to neglect temperature effects. The fitted gain values were

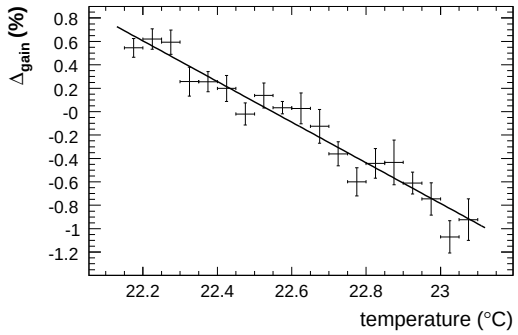

(a) LED 5

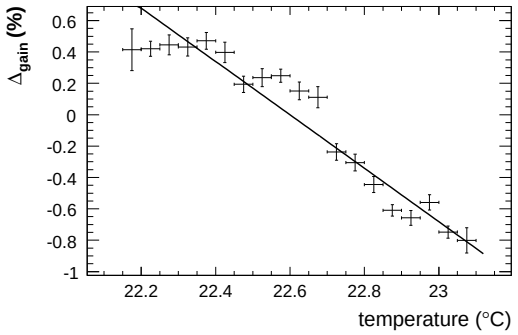

(b) LED 7

Figure 4.9: Variance of the SiPM gain with temperature

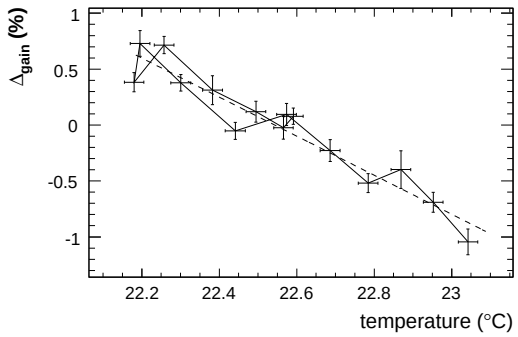

(a) LED 5

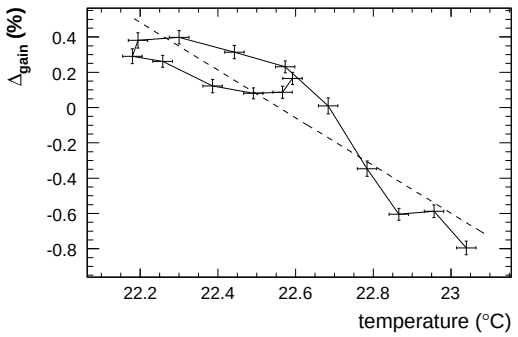

(b) LED 7

Figure 4.10: Measured gain grouped in 10 measurements and linked in the order of their measurement.

histogrammed, and the histograms were shifted in such a way that the mean was zero for all groups. After this correction of the temperature effects, the histograms were summed up. The width of the resulting Gaussian represents the resolution of the gain measurement. For LED 5 $\sigma = 0.51 \pm 0.02$ % was determined, which means 95% of the measurements are accurate within $2\sigma = 1\%$. LED 7 showed $\sigma = 0.473 \pm 0.008$ % and LED 8 showed $\sigma = 0.83 \pm 0.02$ %. The distribution for LED 8 shows tails to higher values, which one does not expect from a pure Gaussian. This means, that less than 95% of the measurements are accurate within 1.66% as one would expect from the fitted values. Figure 4.11 shows the summed histograms for the LEDs.

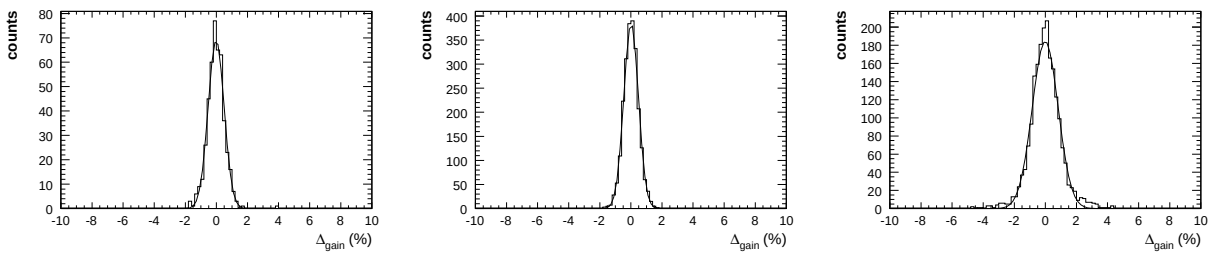

(a) LED 5 (b) LED 7 (c) LED 8

Figure 4.11: Gain measurement fluctuations for the different LEDs.

Summary and Outlook

In this thesis the performance of the readout electronics designed for the analog hadronic calorimeter, and the tailcatcher and muon tracker prototypes was measured. These prototypes use a newly developed silicon based photodetector, called SiPM, and are the first large scale application of this device. As the SiPM is a nonlinear device an exact understanding and a high accuracy of the readout system is necessary to achieve the desired detector resolution.

In a set of measurements it was demonstrated that the individual components answer their purposes. The ASIC chip fulfills the requirements in gain, linearity and noise. The mode covering the full SiPM response shows a maximum nonlinearity of 3% and the signal to noise ratio is 13 for the SiPM design parameters. The mode used for the resolution of single photoelectron spectra has a range linear within 3% that covers signals up to the size of five MIP. The signal to noise for a ideal SiPM is 8.6 in this mode. Also the performance of the integrated DAC satisfies the needs for the individual SiPM voltage adjustments. The maximum voltage error is 50 mV over 95% of the 5 V range and the noise does not exceed 10 mV RMS over 90% of the range. On the side of the data acquisition system, the noise was analyzed and found to be negligible. The differential nonlinearity of the analog to digital converter in the data acquisition was studied and showed no severe effect on the later analysis of the signals.

In addition to these measurements of common parameters, some attributes were measured that are special to the use of the combined system, including the influence of the limited time resolution of the hold signal and the consequences of signals with variable signal shape. The operation mode of the amplifier which is intended for the resolution of single photo electron spectra shows a gain dependence on the input signal shape. As a consequence the ratio between ASIC gains in this and the mode used for beam data taking has to be measured for each channel. The individual calibration of each channel also eliminates the influence of the limited time resolution.

Furthermore, an algorithm was developed for the determination of the SiPM gain from single photoelectron spectra that were recorded with the detector readout electronics. Particular effort was made to ensure that the developed method can be run independently from human intervention, as it is necessary in a 8000 channel system.

The accuracy and stability of the gain measurement was checked with actual data from the first available hadronic calorimeter modules and a set of requirements for a measurement of 1% accuracy was fixed. The established gain measurement was used in the

calibration of modules with cosmic muons. The results proof that the method reaches the expected accuracy, even with the actual available SiPM which do reach a signal to noise ratio of approximately 4. Also the temperature dependence of the SiPM gain of $1.7\frac{\%}{K}$ could be verified with an accuracy of 0.2 percent points.

At the moment the assembly of the AHCAL and TCMT prototypes is ongoing. The combined running of AHCAL and TCMT was successfully demonstrated on a setup with one AHCAL and one TCMT module. The recording of first hadronic showers is planned at a CERN test-beam from August to October 2006. This standalone data taking will be followed by a combined data taking with ECAL, AHCAL and TCMT in October 2006.

Also first experiences were made regarding the use of the data acquisition at the Fermilab Meson Test Beam Facility, which is also a planned site for hadron data taking.

Bibliography

[1] R. Wigmans, *Calorimetry Energy Measurement in Particle Physics*, Oxford University Press, 2000, ISBN 0-19-850296-6.

[2] T. Behnke, *ILC Detector Concepts*, Presentation given at *LCWS 2005*, 18. March 2005, `www-conf.slac.stanford.edu/lcws05/program/talks/detector_concept.pdf`.

[3] CALICE Collaboration, J. C. Brient, *Silicon-tungsten sampling electromagnetic calorimeter for the TeV electron-positron linear collider* Prepared for 11th International Conference on Calorimetry in High-Energy Physics (Calor 2004), Perugia, Italy, 28 Mar - 2 Apr 2004.

[4] V. Andreev *et al.*, *A high granularity scintillator hadronic-calorimeter with SiPM readout for a linear collider detector*, Nucl. Instrum. Meth. **A540**(2005) 368.

[5] CALICE-UK Collaboration, P. D. Dauncey, *Readout electronics for the CALICE ECAL and tile HCAL* (2002), `hep-ex/0211052`.

[6] CALICE Collaboration, F. Sefkow, *The scintillator HCAL testbeam prototype* Prepared for 2005 International Linear Collider Workshop (LCWS 2005), Stanford, California, 18-22 Mar 2005.

[7] P. Buzhan *et al.*, *An advanced study of silicon photomultiplier*, ICFA Instrum. Bull. **23**(2001) 28.

[8] E. Popova, *Status Report – SiPMs production for the testbeam prototype*, Presentation given at *CALCIE technical review*, 25. February 2005.

[9] B. Dolgoshein *et al.*, *Status Report on Silicon Photomultiplier Development and its Apllications.*

[10] N. Wattimena, *Comissioning of an LED Calibration & Monitoring System for the Prototype of a Hadronic Calorimter*, Diplomarbeit, Universität Hamburg, April 2006.

[11] L. Raux, *et al.*, *DRAFT: H-Cal SiPM ASIC WORKING DOCUMENT*, IN2P3-CNRS - Université Paris-Sud, 28. March 2006, `www.lal.in2p3.fr`.

[12] M. Reinecke, *HCAL Frontend Boards*, Presentation given at *HCAL - Technical Meeting*, 24. February 2005.

[13] M. Reinecke, *HCAL Readout Boards - User Manual*, DESY, 30. March 2005.

[14] CALICE Collaboration, P. D. Dauncey, *CALICE electromagnetic calorimeter readout status* (2004), `hep-ex/0410001`.

[15] CAEN S.p.A Costruzioni Apparecchiature Elettroniche Nucleari, *datasheet for CAEN V785N*, 2006, `http://www.caen.it/nuclear/product.php?mod=V785N#`.

[16] burster, *Hochpräzisions-Kalibrierquelle für Spannung, Strom und Thermoelemente – DIGISTANT Typ 4462*, December 2003.

[17] Texas Instruments, *ADS8361 – Dual, 500kSPS, 16-Bit, 2+2 Channel, Simultaneous Sampling ANALOG-TO-DIGITAL CONVERTER*, revised september 2004 edition, August 2002, `www.ti.com`.

[18] R. Brun, *ROOT an Object-Oriented Data Analysis Framework*, `http://root.cern.ch/`.

[19] D. E. Groom, F. James, and R. Cousins, *Probability: in Review of Particle Physics (RPP 2000)*, Eur. Phys. J. **C15**(2000) 191.

[20] W. R. Leo, *Techniques for Nuclear and Particle Physics Experiments: A How-to Approach*, Springer-Verlag Berlin Heidelberg, second revised edition edition, 1994, ISBN 0-387-57280-5.

[21] H. Spieler, *Semiconductor Detector Systems*, Oxford University Press Inc., 2005, ISBN 0-19-852784-5.

[22] *Memorandum of Agreement between the members of the CALICE Collaboration*, 19. July 2005, `http://polywww.in2p3.fr/flc/MOA.pdf`.

[23] A. Dyshkant *et al.*, *Studies of NICADD extruded scintillator strips* FERMILAB-CONF-05-243.

[24] D. Beznosko, A. Bross, A. Dyshkant, A. Pla-Dalmau, and V. Rykalin, *FNAL-NICADD extruded scintillator* Prepared for 2004 IEEE Nuclear Science Symposium and Medical Imaging Conference (NSS / MIC), Rome, Italy, 16-22 Oct 2004.

[25] S. Valkar *et al.*, *A calorimeter for the e+ e- TESLA detector: Proposal for R&D* DESY-PRC-RD-01-02.

[26] E. Garutti, *private communications.*

[27] M. Groll, *private communications.*

[28] N. D'Ascenzo, *private communications.*

[29] P. Goettlicher, *private communications.*

[30] A. Vogel, *private communications.*

[31] M. Reinecke, *private communications.*

[32] E. Garutti, M. Groll, A. Karakash, and S. Reiche, *Magnetic field dependence studies for silicon photomultiplier* LC-DET-2004-025.

[33] M. Danilov, *Tile SiPM production and test status*, Presentation given at *HCAL main meeting*, 7. July 2005.

[34] P. Buzhan *et al.*, *Silicon photomultiplier and its possible applications*, Nucl. Instrum. Meth. **A504**(2003) 48.

[35] N. D'Ascenzo, *Characterization of Silicon Photomultiplier as a photodetector for Positron Emission Tomography*, Master's thesis, University of Pisa, 22. July 2005.

[36] CALICE Collaboration, J. C. Brient, P. Dauncey, and F. Sefkow, *Proposal for SPS beam time for the CALICE calorimeter prototypes* CERN-SPSC-2005-036.

[37] CALICE Collaboration, F. Sefkow, *Performance goals and design considerations for a linear collider calorimeter* Prepared for 11th International Conference on Calorimetry in High-Energy Physics (Calor 2004), Perugia, Italy, 28 Mar - 2 Apr 2004.

List of Figures

List of Tables

Erklärung

Hiermit versichere ich, die vorliegende Arbeit selbständig und nur unter Verwendung der angegebenen Quellen und Hilfsmittel verfasst zu haben. Ich gestatte die Veröffentlichung dieser Arbeit.

Benjamin Lutz